EINDHOVEN UNIVERSITY OF TECHNOLOGY

Eindhoven University of Technology

MASTER

Analysis and modelling of MSM and Schottky barrier GaN UV detectors

Vanhove, N.

Award date:
2005

Link to publication

Disclaimer
This document contains a student thesis (bachelor's or master's), as authored by a student at Eindhoven University of Technology. Student theses are made available in the TU/e repository upon obtaining the required degree. The grade received is not published on the document as presented in the repository. The required complexity or quality of research of student theses may vary by program, and the required minimum study period may vary in duration.

General rights
Copyright and moral rights for the publications made accessible in the public portal are retained by the authors and/or other copyright owners and it is a condition of accessing publications that users recognise and abide by the legal requirements associated with these rights.

- Users may download and print one copy of any publication from the public portal for the purpose of private study or research.
- You may not further distribute the material or use it for any profit-making activity or commercial gain

Analysis and modelling of MSM and Schottky barrier GaN UV detectors

Master Thesis

Nico Vanhove

October 2005

Eindhoven University of Technology (TU/e)
Department of Applied Physics

TU/e technische universiteit eindhoven

Interuniversity Micro-Electronics Center (IMEC)
Advanced Research and Technology (MCP/ART)

Supervisors:
dr. Joachim John (IMEC)
dr. J.E.M. Haverkort (TU/e)

Abstract

Due to the wide bandgap of III-nitrides like GaN (E_g = 3.4 eV), these semiconductors are the most promising candidates to prepare visible-blind ultraviolet (UV) detectors. Nevertheless, the lack of good quality p-type material and low-resistance ohmic contacts are the reason to choose metal-semiconductor-metal (MSM) structures as first option to fabricate UV photodetectors.
In this study, a complete electrical and optical characterization of MSM and Schottky barrier photodetectors is performed to reveal the physical mechanisms which are responsible for the dark current and photocurrent transport phenomena.
The dark current is almost completely determined by the GaN-on-sapphire wafer quality and the metal-semiconductor interface. If a high density of traps caused by interface or defect states is present , trap-assisted tunneling will dominate the dark current characteristics. Otherwise, the thin surface barrier (TSB) model can quantitatively and qualitatively explain and fit the measured dark currents. This barrier is possibly thinned by nitrogen vacancies which act as donors and therefore will enhance tunneling currents.
On the other hand, the photocurrent is composed of two current contributions. The primary current is caused by the thermionic emission or thermionic-field emission of photo-generated charge carriers. The secondary photocurrent contribution is caused by the Schottky barrier lowering due the interface or defect states which can trap charge carriers and therefore disturb the charge neutrality condition.
The effect of annealing on the Schottky parameters and also the promising results of indium-tin-oxynitride (ITON) are discussed in detail. Probably, as-deposited ITON films can chemically passivate the nitrogen vacancies and therefore ITON/n-GaN Schottky barrier photodetectors show the smallest reverse saturation current density compared to Au, Ni and ITO.

Contents

1 Introduction **1**

2 Theory **3**
2.1 Gallium Nitride and his Properties . . . 3
2.2 Ultraviolet Radiation . . . 5
2.2.1 UV Photodetection . . . 5
2.2.2 Photodetector Configurations . . . 6
2.3 Metal-Semiconductor-Metal Photodetectors . . . 7
2.3.1 Theory of Metal-Semiconductor Contacts . . . 7
2.3.2 Operation Principle of a MSM Photodetector . . . 13
2.3.3 Dark Current Mechanisms in MSM Photodetectors . . . 15
2.3.4 Photocurrent Mechanisms in MSM Photodetectors . . . 23
2.4 Comparison of Schottky Barrier Diode and the P-N Junction Diode . . 27

3 Results and Discussion **31**
3.1 Fabrication of MSM and Schottky Barrier Photodetectors . . . 31
3.2 Dark Current Mechanisms in MSM Photodetectors . . . 33
3.2.1 Global Description Dark Current . . . 34
3.2.2 Schottky Parameter Determination in MSM Photodetectors . . . 36
3.2.3 Modelling of the Dark Current Mechanisms . . . 45
3.3 Photocurrent Mechanisms in MSM Photodetectors . . . 53
3.4 The Effect of Annealing on metal/n-type GaN Schottky Barrier Diodes 58

4 Conclusions and Outlook **71**

References **75**

A Detailed Process Flow Photodetectors **79**
A.1 MSM Photodetectors . . . 79
A.2 Schottky Barrier Photodetectors . . . 80

B IGOR Pro Procedure Files **82**
B.1 Thermionic Emission with Barrier Lowering . . . 82
B.2 Thermionic-Field Emission . . . 83

B.3 Thin Surface Barrier (TSB) model 83

Chapter 1

Introduction

Since the beginning of the 19th century, the ultraviolet (UV) region of the electromagnetic spectrum was subject of increasing investigation because in 1801 J.W. Ritter discovered that certain chemical reactions were catalyzed by exposure to non-visible radiation with a shorter wavelength than violet. The sun in the most powerful UV source and the determination of the effects of the various UV solar bands (UV-A, UV-B and UV-C) on the ecosystem and on the human beings is an important subject, and therefore this is the driving force to achieve reliable and efficient UV detectors.
Nowadays, there is a wide range of applications and studies around the UV region. For example UV astronomy, human health, solar observation, flame detection, missile plume detection, pollution monitoring and so on.

A variety of UV detectors are available but mainly Si-based photodetectors and photomultiplier tubes (PMTs). Nevertheless, these photodetectors suffer from significant limitations like the need of filters to absorb low energy photons or the need of a high voltage supply. To pass these limitations, UV detectors based on wide bandgap semiconductors have been studied during the last decade. Therefore, diamond (E_g = 5.4 eV (227 nm)) and SiC (E_g = 2.9 eV (433 nm)) photodetectors were developed. Nevertheless, the hardness of diamond and the relative small bandgap of SiC to make visible-blind UV detectors are serious disadvantages for these photodetectors. Therefore, the development of III-nitride semiconductors like InN, AlN and GaN was a milestone to prepare visible-blind UV detectors. These III-nitrides are direct bandgap materials with GaN showing its absorption edge at 365 nm (E_g = 3.4 eV) and AlN at 200 nm (E_g = 6.2 eV). The tunability of the detection edge by a proper selection of the Al mole fraction (x) in Al_xGa_{1-x} and the already commercial available III-nitride technology for blue light emitting diodes are two important points that have made III-nitride semiconductors to the most adequate solution for UV detection.

In the Microsystems, Components and Packaging (MCP) division of IMEC (Interuniversitair Micro-Elektronica Centrum) situated in Leuven (Belgium), a visible or solar-blind UV focal plane array is going to be fabricated (256 $\times$ 256 pixels).

These UV imaging cameras have to meet some important requirements like true solar-blind operation, high quantum efficiency, low noise (low dark current), high operation speed, UV/visible contrasts larger than four orders of magnitude etc. A second major concern is the connection of the pixels to a readout integrated circuit (ROIC). This has to be done by through-the-wafer hybrid integration because backside UV illumination limits the detector performance. This involves the construction of a hybrid array using a ROIC and a top-illuminated GaN MSM or Schottky barrier diode array with via-holes to the backside of the array for interconnecting to the ROIC.
The aim of this thesis is to perform a complete electrical and optical characterization of one pixel of the intended UV camera to investigate the physical mechanisms which are responsible for the dark- and photocurrent.

Chapter 2

Theory

2.1 Gallium Nitride and his Properties

The Gallium Nitride (GaN) material is at different ways totally different from conventional semiconductors like Si or GaAs. This is mostly related to the material growth itself, which is mostly heteroepitaxial. Because GaN substrates are not available, growth on different materials like sapphire or SiC is necessary. The lattice mismatch that exists between these materials and GaN results in dislocation densities in the order of 10^8-10^{10} /cm^2. In contrast to these large densities in GaN, e.g. GaAs has typical dislocation densities of 10^2-10^4 /cm^2.

Usually, GaN has a wurtzite structure that consists of alternating biatomic closely-packed planes of Ga and N pairs stacked in an ABAB sequence (figure 2.1). Almost all GaN work is done on crystals grown along the c-axis ([0001] direction). Crystals with this orientation have the so-called Ga-face polarity, crystals grown in the $[000\bar{1}]$ direction possess N-face polarity. The definition of polarity is related to the Ga-N bonds parallel to the c-axis. In Ga-face crystals, the Ga atom is above the N atom, for N-face crystals we have the opposite. This distinction is important because most GaN structures are grown on a foreign substrate. In addition, crystals with different polarities also behave differently. The most important material properties of GaN are given in table 2.1.

The best substrate for GaN growth is GaN itself. Due to the high melting point of GaN (2573 K), bulk material growth techniques like Czochralski are not possible. Therefore, GaN substrates are not commercially available on a large scale. Most of the work on GaN is therefore done on heteroepitaxial material, usually using sapphire and SiC as substrates. This approach includes two problems, the mismatch in crystal symmetry and in lattice constants between GaN and the substrate. This is solved by using a thin AlN or GaN buffer (nucleation) layer grown at a low temperature (400 - 600°C), which forms a transitions between the substrate and the GaN layer.

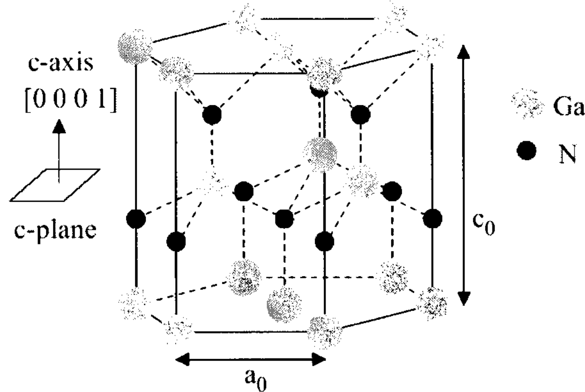

Figure 2.1: GaN wurtzite crystal structure (Ga-face polarity)

Energy Bandgap	3.39 eV
Electron affinity	4.1 eV
Electron mobility	1350 cm^2/Vs
Hole mobility	13 cm^2/Vs
Thermal conductivity	2.1 W/cmK
Electron mass	0.22 m_0
Dielectric constant	9.5
Lattice constants a_0 c_0	 0.3188 nm 0.5185 nm
Melting point	> 2573 K (at 60 kbar)

Table 2.1: GaN material properties at 300K [1]

Metal-organic chemical vapor deposition (MOCVD) and molecular beam epitaxy (MBE) are the common methods used for GaN heteroepitaxy. Trimethylgallium and ammonia are the precursors for the MOCVD growth of GaN. Both hydrogen and nitrogen can be used as carrier gas. The deposition temperature varies between 1000 and 1200°C, which is larger than for MBE (600 - 800°C). In MBE, a solid source is used for Ga, while plasma sources are used to create atomic nitrogen. The growth rates of the methods are about 1 μm /hr.

Sapphire and SiC are the most used substrates for GaN heteroepitaxy. However, both of these substrates suffer from substantial drawbacks. In particular, the lattice constant mismatch between sapphire and GaN is about 16 % and in addition the thermal expansion coefficients of the two materials are poorly matched, which can result in cracking of both the substrate and the epilayer. SiC, on the other hand, exhibits a much reduced lattice constant mismatch to GaN of only about 3.1 %, but its thermal

expansion coefficient is similarly poorly matched to that of GaN. In addition, it is rather expensive and hence not ideal for industrial fabrication.

2.2 Ultraviolet Radiation

Ultraviolet (UV) radiation occupies the spectral interval between 10 nm and 400 nm. It is a highly ionizing, which activates many chemical processes . The most important natural UV source in the sun. UV radiation is commonly divided into three regions [2], as a function of its effects on the biosphere:

- UV-A (400-320 nm): This is the less energetic range. It stimulates photosynthesis, and is involved in the synthesis of some vitamins and basic biochemical compounds. Overexposure can also lead to erythema (skin reddening called sunburn).
- UV-B (320-280 nm): Although partially absorbed by the ozone layer, this composes 10 % of the total UV radiation reaching the earth's surface. UV-B exposure is dangerous for human beings, because its causes skin cancer, cataracts and burns.
- UV-C (280-10 nm): This is the most energetic range, and it is also the most harmful one. However, it is almost completely absorbed by the ozone layer.

Another widespread division of the UV radiation is the following one: near-UV, 400-300 nm; middle-UV. 300-200 nm; far-UV, 200-100 nm; extreme-UV, 100-10 nm.

2.2.1 UV Photodetection

Traditionally, photomultiplier tubes (PMTs), thermal detectors, narrow-band gap semiconductor photodiodes or charge-coupled devices (CCDs) are used for UV detection. PMTs have high gain, low noise and can be visible-blind. However, they are fragile and large instruments, requiring high power supplies. Thermal detectors (pyrometers and bolometers) are commonly used for calibration in the UV range. Although useful as radiometric standards, these detectors are slow and their response is wavelength-independent.
On the other hand, semiconductor photodiodes offer some advantages. They are small, lightweight, insensitive to magnetic fields, cheap, very sensitive and have capabilities to operate at high speed. Due to widespread research and their well-established technology, silicon photodetectors are the most common ones, although GaAs- and GaAsP-based photodiodes are also available.

However, Si-based detectors suffer from their indirect and low bandgap (1.12 eV). Therefore, silicon photodetectors usually have low quantum efficiencies (conversion of photons in electron-hole pairs) and a peak response around 1100 nm, so that external filtering is needed to block the visible and infrared components to make a solar-blind

UV detector. These 'UV enhanced' Si photodetectors use filters which also degrades in space due to radiation damage. Another important drawback for these narrow-bandgap photodetectors is ageing, due to overexposure to radiation of much higher energy than the semiconductor bandgap. Finally, for high-sensitivity applications, the detector must be cooled to reduce the dark current.[2]

UV photodetectors based on wide-bandgap (WBG) semiconductors (diamond, SiC, III-nitrides) can surmount many difficulties listed above. The wide bandgap itself is an important advantage because its enables room-temperature operation and provides visible-blindness. Also the thermal conductivity of WBG materials is in general much better than for Si, which makes high-temperature applications possible. Another advantage is the strength of their chemical bonds, which results in increased radiation hardness. Due to their distinct advantages, we will focus only on WBG semiconductor photodetectors in the following sections.

2.2.2 Photodetector Configurations

In all semiconductor photodetectors the general operation principle is the same. The incoming photons are absorbed in the semiconductor where they create electron-hole pairs. These photo-generated carriers are separated by an electrical field, due to either the built-in potential or the applied voltage, and produce a current proportional with the incoming photon flux.
There are different configurations of semiconductor photodetectors: photoconductors, Schottky barrier photodiodes, metal-semiconductor-metal (MSM) photodiodes, metal-insulator-semiconductor (MIS) structures, p-n and p-i-n photodiodes, and field-effect and bipolar phototransistors. The schematic structures of these devices is visible in figure 2.2.

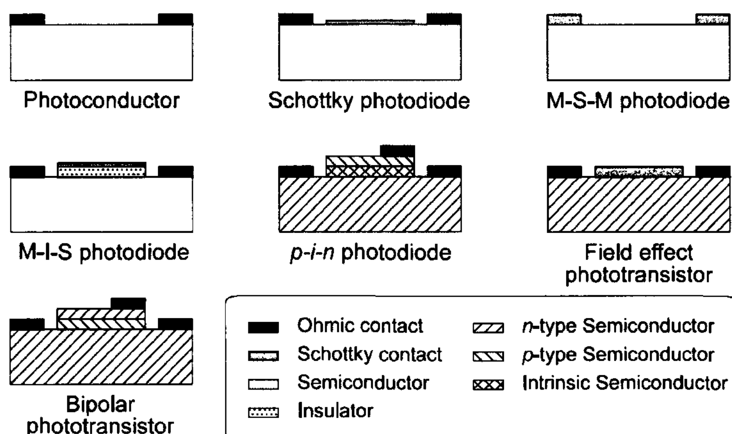

Figure 2.2: Schematic structures of different semiconductor photodetectors [2]

Nevertheless, not all of the above listed structures are possible configurations in WBG photodetectors. Doping of WBG semiconductors is the most important limitation in these materials. For example in GaN, n-type causes never a problem because as-grown material has often unintentional n-type conductivity. The cause of that is still widely debated. Some researchers attribute the n-type conductivity to nitrogen vacancies, which act as donors. Others indicate the unintentional incorporation of silicon and oxygen impurities as the most plausible explanation for n-type conductivity. At the moment, n-type doping with electron concentrations above 10^{19} cm^{-3} can be achieved. On the other hand, p-type doping in GaN is much more difficult to achieve. The most important reason is the high ionization energy of a dopant [3]. This limits the doping efficiency: for instance, the ionization energy of Mg in GaN (around 200 meV) is so large that at room temperature only about 1 % of Mg atoms are ionized. Therefore, the ionization energy determines the fraction of dopants that will contribute free carriers. This means that a Mg concentration of 10^{20} cm^{-3} only leads to a hole concentration of about 10^{18} cm^{-3}. Hence, it is necessary to inject large quantities of the doping impurity to achieve reasonable carrier concentrations, which turn into a reduction on the carrier mobility. Ionization energies are largely determined by the properties of the semiconductor, such as effective masses, dielectric constant, etc.

Another challenge in WBG semiconductors is the development of reliable processes for the fabrication of contacts. Here, the major difficulty is the deposition of low-resistance ohmic contacts, due to the large barrier height by most metals and the limitations to achieve high doping levels.
Due to these difficulties, MSM photodiodes are the first choice to make an UV photodetector because they do not suffer from p-type semiconductors and ohmic contacts. In the next session, the theory of these devices will be discussed in detail.

2.3 Metal-Semiconductor-Metal Photodetectors

In this section, the metal-semiconductor-metal (MSM) photodetectors will be discussed in detail. Normally the structure of a MSM photodetector consists of two interdigitated Schottky contacts connected back-to-back. Therefore, this section will start with a detailed overview of the Schottky theory. Afterwards, the operation principle of the MSM photodetector will be given with a comprehensive description of the different conduction mechanisms which play a role in the dark- and photocurrent.

2.3.1 Theory of Metal-Semiconductor Contacts

In figure 2.3, a diagram is shown of a metal-semiconductor contact with flat bands (no equilibrium) and one in equilibrium where band bending occurs. The band structures in this figure are shown for a n-type semiconductor with a work function less than that of the metal.

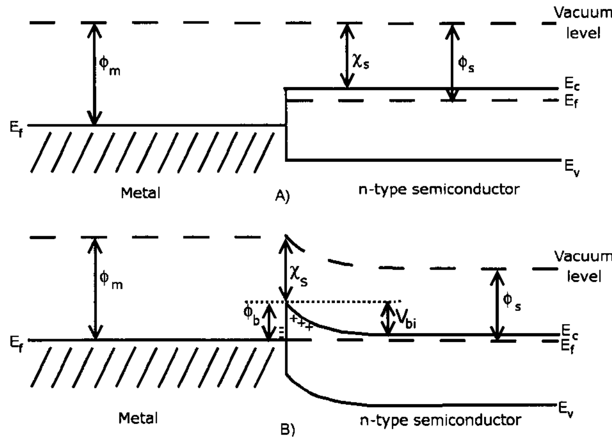

Figure 2.3: Band diagram of a metal-semiconductor contact: A) non-equilibrium state B) equilibrium state (symbols explained in text)

The flatband diagram is not a thermal equilibrium diagram, since the Fermi energy in the metal differs from that in the semiconductor. Electrons in the n-type semiconductor can lower their energy by traversing the junction. As the electrons leave the semiconductor, a positive charge, due to the ionized donor atoms, stays behind. This charge creates a negative field and lowers the band edges of the semiconductor. Electrons flow into the metal until equilibrium is reached between the diffusion of electrons from the semiconductor into the metal and the drift of electrons caused by the field created by the ionized impurity atoms. This thermal equilibrium is characterized by a constant Fermi level throughout the structure.

The parameter ϕ_B is the ideal barrier height of the semiconductor contact, the potential barrier seen by electrons in the metal trying to move into the semiconductor and according to the Schottky-Mott theory [4] ϕ_B can be expressed as follows:

$$\phi_B = \phi_m - \chi_s \tag{2.1}$$

where ϕ_B is the barrier height at zero applied bias, ϕ_m is the work function of the metal and χ_s is the electron affinity of the semiconductor and is expressed as:

$$\chi_s = \phi_s - (E_c - E_f) \tag{2.2}$$

where ϕ_s is the work function of the semiconductor, E_c the conduction band energy and E_f the Fermi level energy.
On the semiconductor side, V_{bi} is the built-in potential barrier seen by electrons in the conduction band trying to move into the metal and is given by:

$$V_{bi} = \phi_m - \phi_s = \phi_B - (E_c - E_f) \tag{2.3}$$

When an abrupt metal-semiconductor transition is assumed (full depletion approximation), the magnitude of the electric field (ε) in the space charge region can be determined from Gauss's law:

$$\frac{d\varepsilon}{dx} = \frac{\rho(x)}{\epsilon_s} \tag{2.4}$$

where $\rho(x)$ the space charge volume density and ϵ_s the semiconductor permittivity. Assuming a uniform semiconductor doping, the electric field increases linearly as the metal is approached, rising from zero at $x = W$ to a value of qN_dW/ϵ_s at the interface by:

$$|\varepsilon(x)| = \frac{qN_d}{\epsilon_s}(W - x) = \varepsilon_m - \frac{qN_d}{\epsilon_s}x \tag{2.5}$$

where N_d the doping concentration and ε_m the maximum field strength which occurs at $x = 0$.

The space-charge in the depletion zone (qN_dW) in the n-type semiconductor equals the surface charge. Therefore, the width of the depletion zone (W) is the same as in p-n junctions, where a high p-doping is assumed (a p^+-n junction):

$$W = \sqrt{\frac{2\epsilon_s}{qN_d}\left(V_{bi} - V - \frac{k_BT}{q}\right)} \tag{2.6}$$

The space charge Q_{sc} per unit area of the semiconductor and the depletionlayer capacitance C per unit area are given by:

$$Q_{sc} = qN_dW = \sqrt{2q\epsilon_sN_d\left(V_{bi} - V - \frac{k_BT}{q}\right)} \tag{2.7}$$

$$C = \frac{|\partial Q_{sc}|}{\partial V} = \sqrt{\frac{q\epsilon_sN_d}{2(V_{bi} - V - k_BT/q)}} = \frac{\epsilon_s}{W} \tag{2.8}$$

Eqn. 2.8 can be written in the form:

$$\frac{1}{C^2} = \frac{2(V_{bi} - V - k_BT/q)}{q\epsilon_sN_d} \tag{2.9}$$

Therefore, if N_d is constant throughout the depletion zone, a straight line should obtained by plotting $1/C^2$ versus V.

This theory is not complete because it assumes ideal conditions where dipole surface contributions do not change the barrier height when the metal and the semiconductor are in contact [5]. It also assumes that there are no interfacial layers or physical strains created between the two when they are brought into contact.

In practice, however, surface dipole layers do arise because at the surface of a solid the atoms have neighbors on one side only (dangling bonds) (see figure 2.4). This causes a distortion of the electron cloud belonging to the surface atoms. Also experimentally was discovered that ϕ_B is less dependent on ϕ_m in contradiction to eqn. 2.1.

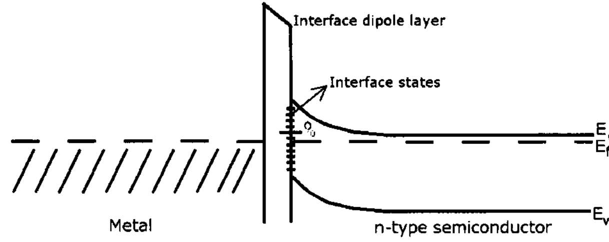

Figure 2.4: Metal-semiconductor contact with an interface dipole layer and interface states with neutral level ϕ_0

One explanation of this weak dependence is given in terms of localized surface states or "dangling bonds". The surface states are continuously distributed in energy within the forbidden gap and are characterized by a neutral level, ϕ_0, such that if the surface states are occupied up to ϕ_0 and empty above ϕ_0, the surface is electrically neutral (see figure 2.4).
In general, the Fermi level does not coincide with the neutral level. In this case, there will be a net charge in the surface states. If in addition (and often in practice due to chemical cleaning of the semiconductor prior to processing) there is a thin oxide layer between the metal and the semiconductor, the charge in the surface states together with its image charge on the surface of the metal will form a dipole layer. This dipole layer will change the potential difference between the semiconductor and the metal. The modification to the Schottky-Mott theory is expressed as [5]:

$$\phi_B = \gamma(\phi_m - \chi_s) + (1-\gamma)(E_g - \phi_0) \tag{2.10}$$

where E_g the bandgap of the semiconductor and ϕ_0 the position of the neutral level and γ expressed as:

$$\gamma = \frac{\varepsilon_i}{\varepsilon_i + q\delta D_S} \tag{2.11}$$

where ε_i the permittivity of the thin oxide layer, δ the thickness of the oxide layer end D_s the density of the surface states.
Hence if there are no surface states, $D_s = 0$ and $\gamma = 1$ and eqn. 2.10 becomes identical to eqn. 2.1. But if the density of surface states is very high, γ becomes very small and ϕ_B approaches the value $(E_g - \phi_0)$. When this happens, the Fermi level is said to be "pinned" to the band edges by the surface states and therefore becomes independent of the metal work function.

Current Transport in Metal-Semiconductor Contacts

The current transport in a Schottky device is determined by the majority carriers. When the majority carriers (in our case electrons) are arrived at the metal-semiconductor interface, they can be emitted over the barrier into the metal due to thermionic emission.

If a positive voltage to the semiconductor with respect to the metal is applied (reverse bias), the semiconductor-to-metal barrier height increases (see figure 2.5b). If a positive voltage is applied to the metal with respect to the semiconductor (forward bias), the semiconductor-to-metal barrier V_{bi} is reduced (see figure 2.5a). In that situation, electrons can more easily flow from the semiconductor into the metal since the barrier is reduced.

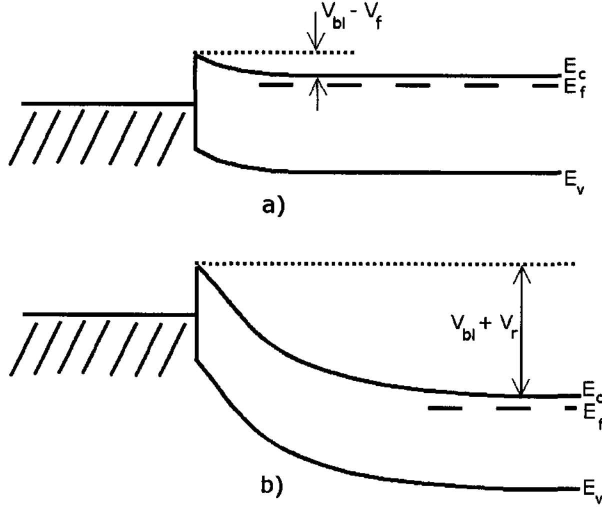

Figure 2.5: Ideal energy-band diagram of a metal-semiconductor contact (a) under forward bias and (b) under reverse bias

The current-voltage characteristic of a Schottky barrier diode can be expressed as:

$$I = AA^{**}T^2 e^{\frac{-q\phi_B}{k_BT}} \left(e^{\frac{-qV}{nk_BT}} - 1\right) = I_s \left(e^{\frac{-qV}{nk_BT}} - 1\right) \tag{2.12}$$

where A is the area of the metal-semiconductor interface, A^{**} the effective Richardson constant, T the temperature, k_B the Boltzmann constant, q the electronic charge, V the applied bias voltage, n the ideality factor and I_s the saturation current.
The ideality factor is a measure of the quality of the junction and is highly process dependent. The value for an ideal Schottky junction is 1. In practice, however, larger values are obtained due to the presence of non-ideal effects or components to the current through the junction.

In addition to thermionic emission, there are a number of other current transport mechanisms which will contribute to the electric properties of the metal-semiconductor interface; the most important one which will be discussed in this section are image force lowering of the barrier height and quantum mechanical tunneling.
The application of an electric field causes the image-force-induced lowering of the potential energy for charge carrier emission. Consider an electron, in vacuum, at a

distance x from a metal surface. A positive charge will be induced on the metal at a distance -x from its surface and will give rise to an attractive force between the two, known as the image force. This force has associated with it an image potential energy which corresponds to the potential energy of an electron at a distance x from the metal. When an external field is applied, together these two energy components have the effect of lowering the Schottky barrier. Thus at high fields, the Schottky barrier is considerably lowered.

These results can be applied to a metal/semiconductor junction. However, the field is now replaced by the maximum field, E_{max}, at the interface. The amount of reduction due to the induced-image-force, $\Delta\phi_B$, is given by (see figure 2.6):

$$\Delta\phi_B = \sqrt{\frac{qE_{max}}{4\pi\epsilon_s}} \tag{2.13}$$

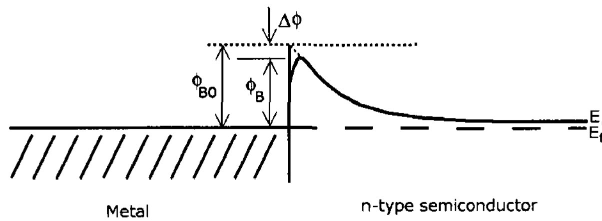

Figure 2.6: Energy-band diagram of a metal-semiconductor contact showing the image-force Schottky barrier lowering $\Delta\phi$ where ϕ_{B0} the flatband Schottky barrier height and ϕ_B the zero-bias Schottky barrier height

Another current-transport mechanism is tunneling through the barrier. Under certain circumstances, electrons with energies below the top of the barrier can penetrate this barrier by quantum-mechanical tunneling. This modify the ordinary thermionic theory in one of these two ways.

In the case of a very heavily doped semiconductor at low temperature, the current in the forward direction arises from the tunneling of electrons with energies close to the Fermi energy in the semiconductor. This is known as field emission.

If the temperature is raised, electrons are excited to higher energies and the tunneling probability increases rapidly because the electrons 'see' a thinner and lower barrier. On the other hand, the number of excited electrons decreases rapidly with increasing energy and there will be a maximum contribution to the current from electrons which have a certain energy above the bottom of the conduction band. This is known as thermionic-field emission.

If the temperature will be further increased, a point is reached where all the electrons will pass the barrier and the effect of tunneling is negligible. In this case, again thermionic emission is the mean current-transport mechanism.

In the reverse direction, tunneling through the barrier becomes more significant at lower doping levels than in the forward direction because the bias voltages involved are usually much larger. Also a moderately large reverse bias can cause the barrier to become thin enough for tunneling of electrons from the metal to the semiconductor, even at low doping levels.
The tunneling current density J_{tun} can expressed by [5]:

$$J_{tun} = -J_s e^{V_r\left(\frac{q}{k_B T} - \frac{1}{E_0}\right)} \tag{2.14}$$

where V_r is the reverse bias voltage and $E_0 = E_{00} \coth\left(qE_{00}/k_B T\right)$. E_{00} is a tunneling parameter related to the material properties of the semiconductor and is expressed as:

$$E_{00} = \frac{qh}{2\pi}\sqrt{\frac{N_d}{m^* \epsilon_s}} \tag{2.15}$$

where m^* the effective mass of electrons in the semiconductor, ϵ_s the permittivity and N_d the donor concentration. The physical significance of E_{00} can be seen as the built-in potential of a Schottky barrier such that the transmission probability for an electron, with the same energy as the bottom of the conduction band at the edge of the depletion region, is equal to e^{-1}. In other words, the ratio $k_B T/qE_{00}$ is a measure of the importance of thermionic emission and tunneling. Field emission is expected if $k_B T \ll qE_{00}$, thermionic-field emission if $k_B T \approx qE_{00}$ and thermionic emission if $k_B T \gg qE_{00}$.
J_s is the tunneling saturation current density and is a slowly varying function of the applied bias given by:

$$J_s = \frac{A^{**} T \sqrt{\pi q E_{00}}}{k_B}\left(q(V_r - V_n) + \frac{q\phi_B}{\cosh^2\left(qE_{00}/k_B T\right)}\right)^{\frac{1}{2}} e^{\frac{-\phi_B}{E_0}} \tag{2.16}$$

where A^{**} is the effective Richardson constant and V_n the potential energy difference between the bulk conduction band and the Fermi level.

2.3.2 Operation Principle of a MSM Photodetector

A MSM photodetector is a Schottky barrier device consisting of interdigitated (finger structures) metal electrodes deposited on a semiconductor substrate. The device detects the presence of light, by converting the incoming photons into an electrical signal. Figure 2.7 displays the cross section of a MSM photodetector, indicating the dimensions, carrier motion, the electric field and the incoming illumination.
s and w refer to the electrode spacing and width, respectively, d to the thickness of the photoactive region and $\vec{E}$ to the electrical field. The common bias points ±V and the generated photocurrent I_{ph} are also indicated.

The photodetector is illuminated from the top with photons whose energy is larger than the bandgap energy of the semiconductor. The amount of photo-generated carriers depends on the photon flux. Light absorption in the semiconductor leads to

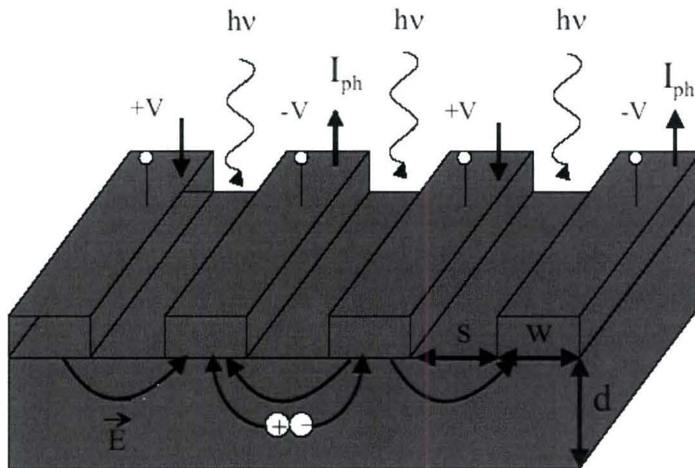

Figure 2.7: Cross section of a MSM photodetector (symbols explained in text)

electron-hole generation. By applying an external bias voltage to the metal contacts, electrons in the conduction band and holes in the valence band are swept into opposite directions. Carriers are then collected at the metal pads and a current, which is proportional to the incoming photon flux, is detected in the external circuit.
When biased, the metal fingers form two Schottky-diodes connected in series; one forward biased, the other reverse biased. As we will see in next sections, the semiconductor is fully depleted in the region between the fingers if the applied bias voltage exceeds the flatband voltage. Therefore, it is important to use active layers with a low doping density to achieve full depletion of majority carriers for reasonable gap spacings. As a result of this, the incoming photons are collected efficiently and the generated electron-hole pairs are quickly swept out of the space-charge region. Furthermore, a low background free electron concentration is necessary to achieve very low dark currents.

Due to the geometry of the interdigitated electrodes, the capacitance of the detector is in the order of fFs, even for relatively large active areas. The series resistance of the fingers can also be kept small by optimizing the length of the fingers and the metal cross section area. Therefore, the RC time is relatively low and does not usually limit the device speed.
Other advantages of MSM structures are its fabrication simplicity and the need of only one active layer; only one metallization is needed to process MSM photodetectors on a single doped n-type layer in our case. MSM structures have also a low dark current density, which is mainly attributed to the leakage of carriers over/through the revered biased Schottky barrier. Therefore, a high Schottky barrier is desirable in order to minimize the dark current. The mechanisms which contribute to the dark current will be discussed in detail in the next section.

2.3.3 Dark Current Mechanisms in MSM Photodetectors

The basic transport process for a Schottky diode with n-type semiconductor under reverse bias without illumination are transport of electrons, that have sufficient energy to overcome the potential barrier. Nevertheless, other mechanisms can play an important role in the electrical properties of the photodetector. The most important one is quantum-mechanical tunneling of electrons through the barrier from the metal into the semiconductor (field or thermionic-field emission), but also generation in the space-charge region, generation in the neutral region or carrier generation supported by states in the forbidden bandgap can influence the properties of the photodetector. The inverse processes occur under forward bias.

The MSM structure has two Schottky barriers connected back-to-back. Therefore, the various current transport processes may deviate from that of a single Schottky diode. The applied voltage has also a important role in determining the current transport characteristics. In the following, different voltage regions are investigated for a n-type MSM photodetector [6].

- **Thermal equilibrium**
  The charge distribution at thermal equilibrium for a MSM photodetector with n-type semiconductor with ionized impurity concentration N_d is shown in figure 2.8(b). The corresponding electrical field and potential distribution are obtained from the integration of the Poisson's equation and are visible in figures 2.8(c) and (d).

  ϕ_{Bn1}, ϕ_{Bn2} are the electron barrier heights, ϕ_{Bp1} and ϕ_{Bp2} are the hole barrier heights and V_{bi1}, V_{bi2} are the built-in potentials at contacts 1 and 2, respectively. The depletion layer widths are:

$$W_{1,2} = \sqrt{\frac{2\epsilon_s}{qN_d} V_{bi1,bi2}} \tag{2.17}$$

  where N_d the donor concentration and $\epsilon_s = \epsilon_r \epsilon_0$ the semiconductor permittivity. For a symmetrical MSM structure (same contact metals): $\phi_{Bn1} = \phi_{Bn2} = \phi_{Bn}$ and $q\phi_{Bn1} + q\phi_{Bp2} = E_g$. Further the built-in voltage $V_{bi1} = V_{bi2} = V_{bi}$:

$$V_{bi} = \phi_{Bn} - \left(\frac{E_c - E_f}{q}\right) = \phi_{Bn} - \frac{k_B T}{q} \ln \frac{N_c}{N_d} \tag{2.18}$$

  where E_c the conduction band energy level, E_f the semiconductor Fermi level, k_B the Boltzmann constant, T the temperature, q the elementary charge and N_c is the effective density of states in the conduction band:

$$N_c = 2\left(\frac{2\pi m_e^* k_B T}{h^2}\right)^{\frac{3}{2}} \tag{2.19}$$

  where m_e^* the electron effective mass. At zero bias no current will flow.

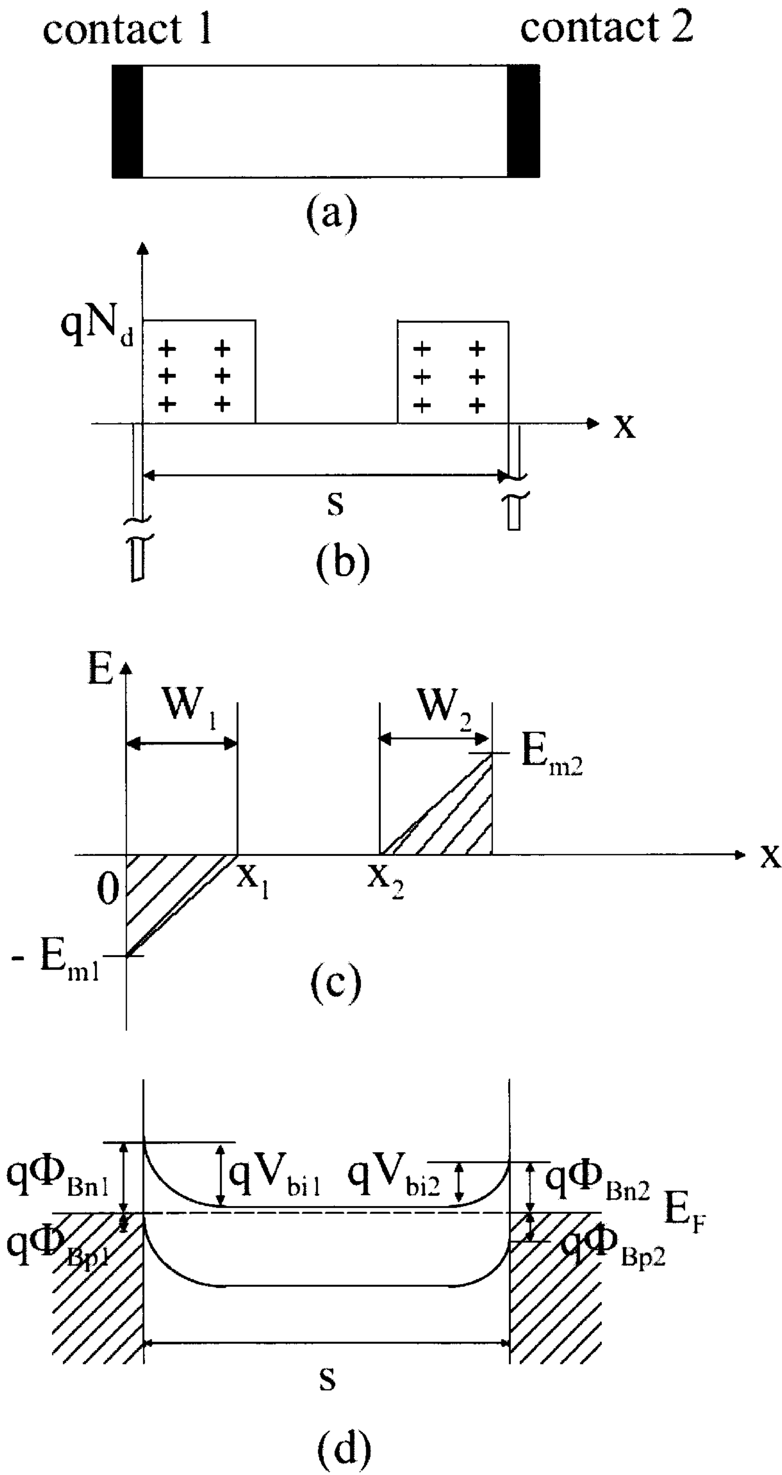

Figure 2.8: (a) Schematic diagram of a MSM photodetector; (b) charge distribution; (c) electrical field; (d) energy band diagram at thermal equilibrium

- **Small voltage range V < V_{RT}**
  The small voltage range applies to voltages below the reach-through voltage V_{RT}, where the depletion widths W_1 and W_2 are smaller than the electrode gap spacing s. The charge distribution, electrical field and energy band profile under low bias are shown in figure 2.9. The contact 1 with a negative voltage with respect to contact 2 is reverse-biased (cathode) whereas contact 2 is forward-biased (anode). qV_1 is the difference between the Fermi level of metal contact 1 to that in the semiconductor; qV_2 is the difference between the Fermi level of metal contact 2 to that in the semiconductor. $V = V_1 + V_2$ is the applied voltage shared between the two contacts.

  From current continuity requirements and assuming that both contacts have the same area: $J_{n1} = J_{n2}$. The electron current density is due to the thermionic emission of electrons from the cathode and is expressed as:

$$J_{n1} = A_n^{**}T^2 e^{-\frac{q}{k_BT}(\phi_{Bn1}-\Delta\phi_{Bn1})}\left(1 - e^{\frac{-qV_1}{k_Bt}}\right) \tag{2.20}$$

  where A_n^{**} the effective Richardson constant for electrons with the corresponding electron effective mass m_e^*:

$$A_n^{**} = \frac{4\pi q m_e^* k_B^2}{h^3} \tag{2.21}$$

  where h the Planck constant and $\Delta\phi_{Bn1}$ is the Schottky barrier lowering or image force lowering due to the applied electric field given by:

$$\Delta\phi_{Bn1} = \sqrt{\frac{qE_{m1}}{4\pi\epsilon_s}} \tag{2.22}$$

  The maximum electric field E_{m1} at the cathode is:

$$E_{m1} = \sqrt{\frac{2qN_d}{\epsilon_s}(V_1 + V_{bi1} - \frac{k_BT}{q})} \tag{2.23}$$

  The origin of the hole current is the thermionic emission of holes from the anode:

$$J_{p2} = A_p^{**}T^2 e^{-\frac{q}{k_BT}(\phi_{Bp2}+V_{bi2}-V_2)} \tag{2.24}$$

  where A_p^{**} the effective Richardson constant for holes with the corresponding hole effective mass and $\phi_{Bp2}+V_{bi2}-V_2$ the effective barrier height. Only injected holes which diffuse from x_2 to x_1 influence the total hole current. Generally, the hole current is much smaller than the electron current. Solving the current continuity equation for holes using the particle and displacement current densities, the hole

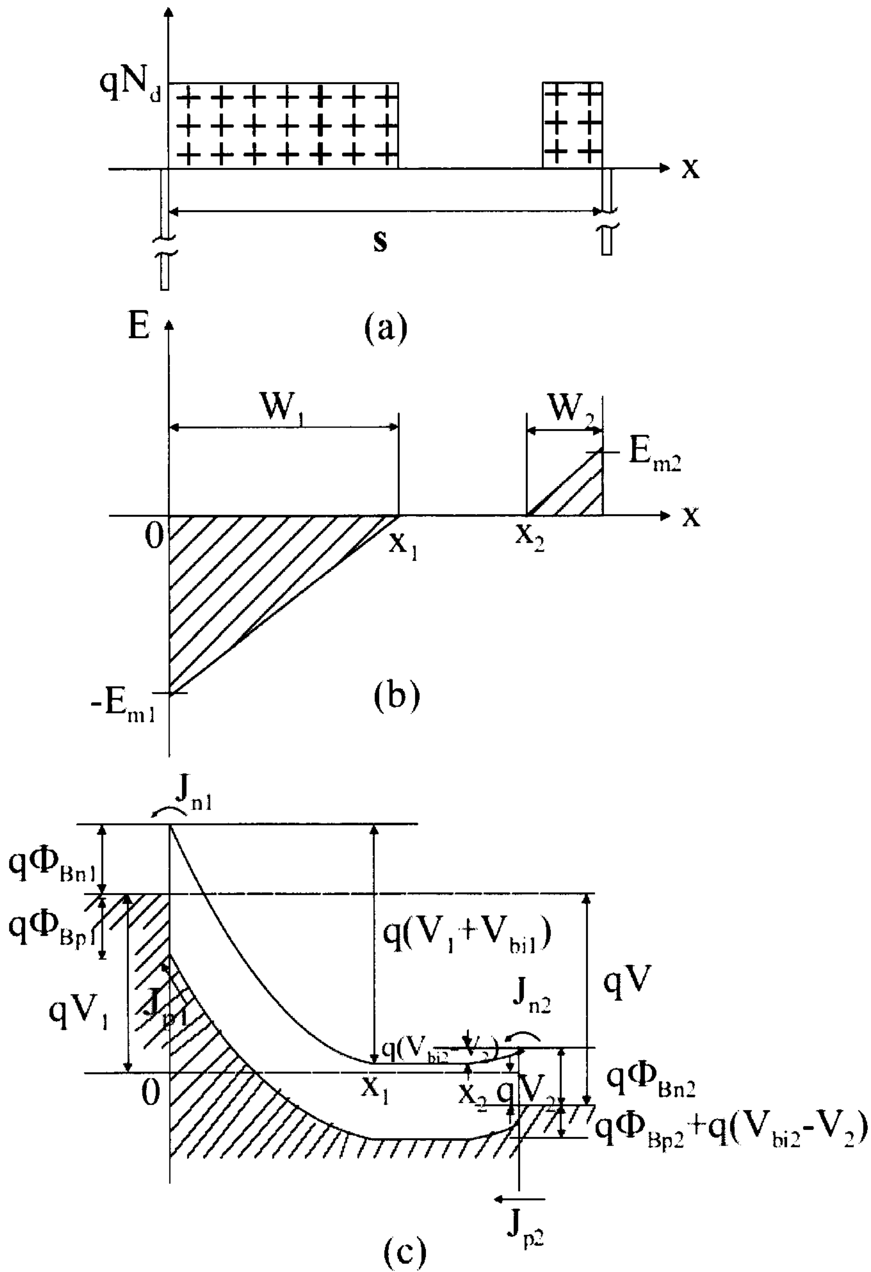

Figure 2.9: (a) charge distribution; (b) electrical field; (c) energy band diagram under low bias (contact 1 reverse-biased)

current density J_{p1} at the cathode:

$$J_{p1} = qD_p \frac{dp}{dx}|_{x1} =$$

$$\frac{qD_p p_{n0} \tanh[(x_2 - x_1)/L_p]}{L_p} \left(1 - e^{-\frac{qV_1}{k_B T}}\right) + \frac{A_p^{**} T^2 e^{\frac{-q}{k_B T}(\phi_{Bp2} + V_{bi2})}}{\cosh[(x_2 - x_1)]/L_p} \left(e^{\frac{qV_2}{k_B T}} - 1\right) \tag{2.25}$$

The total current is the sum of the electron- and hole-currents:

$$J_{dark} = J_{n1} + J_{p1} \tag{2.26}$$

Under low bias, the barrier of holes ($\phi_{Bp2} + V_{bi2} - V_2$) is higher than that of electrons (ϕ_{Bn1}). Therefore, the dominant current component is the reverse electron saturation current.

- **Voltages larger than the reach-through voltage V > V$_{RT}$**
  By increasing the bias voltage, the depleted area at the cathode grows while at the anode it reduces. A small current is injected through the barriers: hole current at the forward biased contact and electron current at the reverse biased contact. The barrier for the holes is rapidly reduced with increasing voltage. Therefore, if the height of a Schottky barrier on n-type material is greater than half the bandgap, the region of the semiconductor adjacent to the metal becomes p-type and contains a high density of holes. These holes will diffuse into the neutral region of the semiconductor under forward bias. In that case, the electron current remains constant but the injected hole current from the forward biased contact begins to increase rapidly as the hole barrier ($\phi_{Bp2} + V_{bi2} - V_2$) is lowered. Nevertheless, the electron to hole current ratio is therefore determined by the bandgap of the semiconductor. The two depletion regions touch each other ate the reach-through voltage. At this moment, the whole MSM structure is depleted. The sum of the depletion regions equals the electrode gap spacing $s = W_1 + W_2$, see figure 2.10.
  For a symmetrical structure $V_{bi1} = V_{bi2} = V_{bi}$, so that the depletion widths are:

$$W_1 = \sqrt{\frac{2\epsilon_s}{qN_d}(V_1 + V_{bi})} \tag{2.27}$$

$$W_2 = \sqrt{\frac{2\epsilon_s}{qN_d}(V_{bi} - V_2)} \tag{2.28}$$

Most of the applied voltage drops across the cathode. Assuming $V_1 = V = V_{RT}$ and $V_2 = 0$ in $W_1 + W_2 = s$, gives for the reach-through voltage:

$$V_{RT} = \frac{qN_d s^2}{2\epsilon_s} - s\sqrt{\frac{2qN_d}{\epsilon_s}V_{bi}} \tag{2.29}$$

Full depletion of the active region can occur even at zero bias, if the electrons spacing s and/or the donor concentration N_d are small enough. By setting $V_{RT} =$

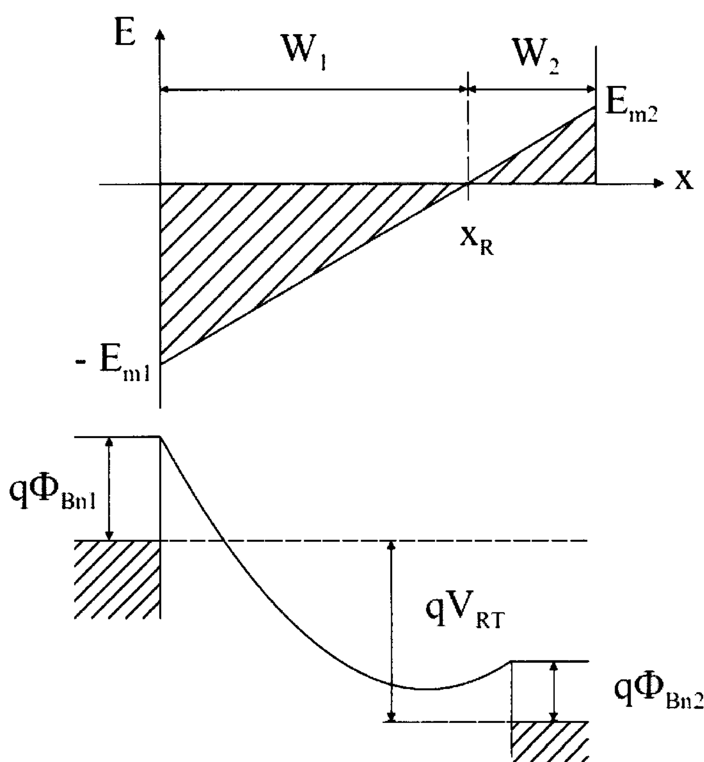

Figure 2.10: Reach-through condition (a) electrical field; (b) energy band diagram

0 or $W_1 + W_2 = s$ using eqn. 2.17, the spacing is defined as $s_{depleted} = \sqrt{\frac{8\epsilon_s V_{bi}}{qN_d}}$. After reach-through, the electric field is continuous and varies linearly from $x = 0$ to $x = s$, see figure 2.11.

The maximum fields at the cathode and anode, respectively, are:

$$E_{m1} = \frac{V + V_{FB}}{s} \tag{2.30}$$

$$E_{m2} = \frac{|V - V_{FB}|}{s} \tag{2.31}$$

where the voltage V_{FB} the flatband voltage which makes the depletion width at the anode $W_2 = 0$. The relation between the applied voltage and the reverse-biased/forward-biased barrier height becomes therefore:

$$V_1 + V_{bi} = \frac{E_{m1}x_r}{2} = \frac{(V + V_{FB})^2}{4V_{FB}} \tag{2.32}$$

$$V_{bi} - V_2 = \frac{E_{m2}(s - x_r)}{2} = \frac{(V_{FB} - V)^2}{4V_{FB}} \tag{2.33}$$

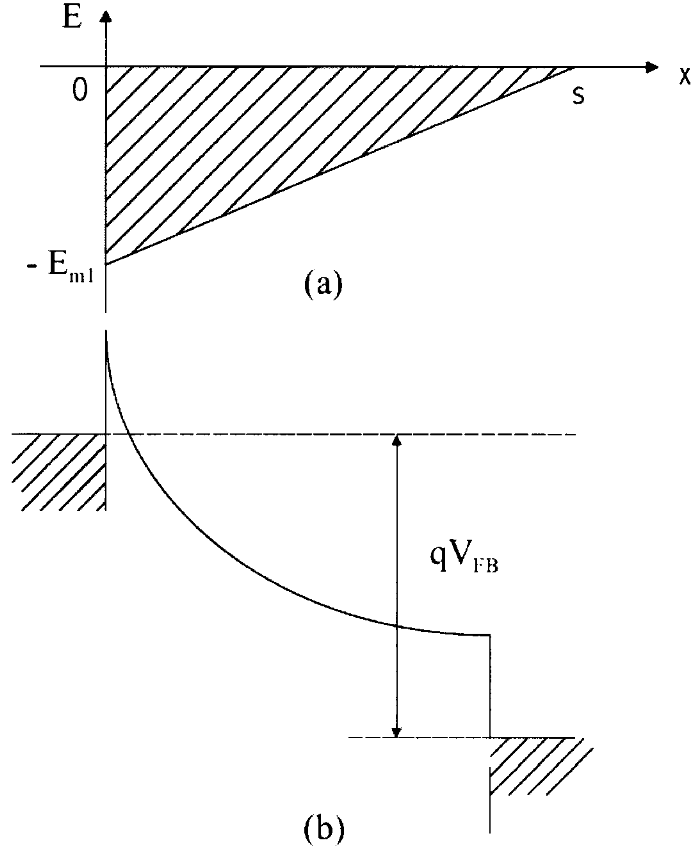

Figure 2.11: Flatband condition (a) electrical field; (b) energy band diagram

where x_r is the reach-through point (the position at which point the electric field is zero): $x_r = \epsilon_s E_{m1}/qN_d = \frac{s(V+V_{FB})}{2V_{FB}}$. When the applied voltage exceeds V_{RT}, the neutral region $(x_2 - x_1)$ becomes zero and eqn. 2.25 using eqn. 2.33 reduces to:

$$\begin{aligned} J_{p1} &= A_p^{**}T^2 e^{\frac{q(\phi_{Bp2}+V_{bi})}{k_B T}} \left(e^{\frac{qV_2}{k_B T}} - 1 \right) \\ &= A_p^{**}T^2 e^{-\frac{q\phi_{Bp2}}{k_B T}} \left(e^{-\frac{q(V_{FB}-V)^2}{k_B T 4 V_{FB}}} - e^{-\frac{qV_{bi}}{k_B T}} \right) \end{aligned} \tag{2.34}$$

The total current is the sum of eqns. 2.20 and 2.34 (note that in eqn. 2.20 the second exponential term drops out, because applying a voltage V_1 it approaches zero):

$$J_{dark} = A_n^{**}T^2 e^{-\frac{q}{k_B T}(\phi_{Bn1}-\Delta\phi_{Bn1})} + A_p^{**}T^2 e^{-\frac{q\phi_{Bp2}}{k_B T}} \left(e^{-\frac{q(V_{FB}-V)^2}{k_B T 4 V_{FB}}} - e^{-\frac{qV_{bi}}{k_B T}} \right) \tag{2.35}$$

From eqn. 2.35, it can be seen that the current increases exponentially with increasing bias voltage.

- **Voltages larger than the flatband voltage V > V_{FB}**
  As the voltage is further increased, the energy band at $x = s$ becomes flat and the electric field becomes zero. This is the flatband condition with the corresponding flatband voltage, V_{FB}. By setting $x_r = s$, the maximum field at the cathode becomes $E + m1 = \frac{sqN_d}{\epsilon_s}$. Equalizing this with eqn. 2.30 gives for the flatband voltage:

$$V_{FB} = \frac{qN_d s^2}{2\epsilon_s} \tag{2.36}$$

By proper selection of N_d and s, the flatband voltage can be varied from a few volts to a tenfold. Increasing the voltage in excess of V_{FB}, causes the energy band to bend further downward, see figure 2.12.

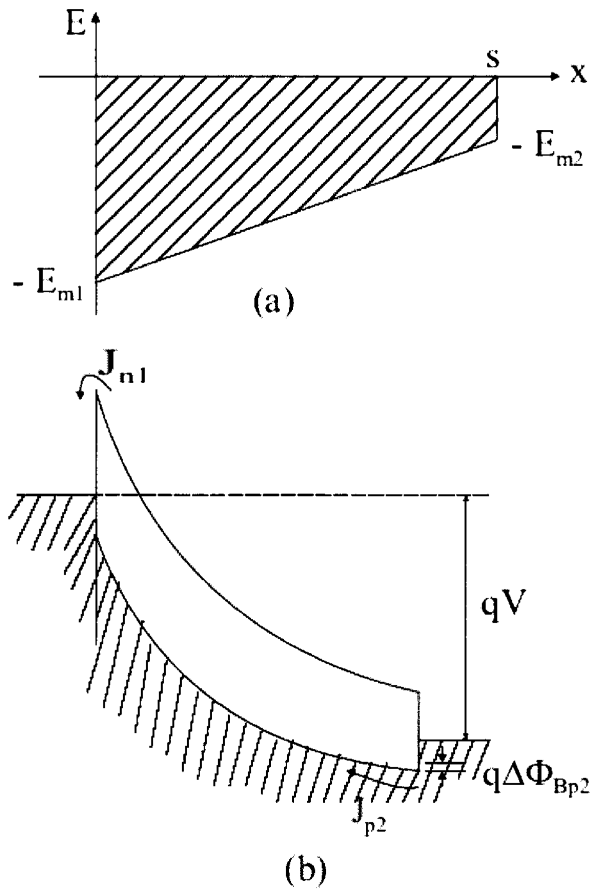

Figure 2.12: Applied voltage larger than V_{FB} (a) electrical field; (b) energy band diagram

The maximum voltage, the breakdown voltage V_{BD}, which can be applied to the MSM structures is limited by the breakdown phenomena near the maximum field at the cathode. Using eqn. 2.30 and defining the maximum field E_{m1} at breakdown as E_{BD} the maximum applicable voltage becomes:

$$V_{BD} = E_{BD}s - V_{FB} \tag{2.37}$$

At $V = V_{FB}$, the factor in brackets in the hole current density, eqn. 2.34, approaches unity. The hole current reaches its critical value since the hole barrier approaches the limiting magnitude ϕ_{Bp2}. For voltages in excess of V_{FB} the hole current increases slowly due to the Schottky barrier lowering effect. The hole current is now expressed as:

$$J_{p1} = A_p^{**}T^2 e^{-\frac{q}{k_B T}(\phi_{Bp2} - \Delta\phi_{Bp2})} \tag{2.38}$$

where $\Delta\phi_{Bp2}$ is the Schottky barrier lowering for holes:

$$\Delta\phi_{Bp2} = \sqrt{\frac{qE_{m2}}{4\pi\epsilon_s}} = \sqrt{\frac{q(V - V_{FB})}{4\pi\epsilon_s}} \tag{2.39}$$

with E_{m2} defined in eqn. 2.31. The total current, assuming that breakdown phenomena can be neglected, is the sum of eqns. 2.20 and 2.38:

$$J_{dark} = A_n^{**}T^2 e^{-\frac{q}{k_B T}(\phi_{Bn1} - \Delta\phi_{Bn1})} + A_p^{**}T^2 e^{-\frac{q}{k_B T}(\phi_{Bp2} - \Delta\phi_{Bp2})} \tag{2.40}$$

2.3.4 Photocurrent Mechanisms in MSM Photodetectors

One of the most important parameters to describe the performance of a MSM photodetector is the responsivity (R). This is the ratio of the generated photocurrent to the incoming illumination with an optical power corresponding to a photon energy $h\nu$ at the wavelength λ:

$$R = \frac{I_{ph}}{P_{opt}} = \frac{q\eta G_i}{h\nu} = \frac{\lambda\eta G_i}{1.24 \times 10^{-6}} \tag{2.41}$$

where η the quantum efficiency of the device and G_i the internal gain. The quantum efficiency for a MSM diode is expressed as:

$$\eta = \eta_i(1 - r)(\frac{s}{s + w})(1 - e^{-\alpha d}) \tag{2.42}$$

where η_i the internal quantum efficiency, r the reflection coefficient at the air-semiconductor interface depending on the material and the wavelength, d the thickness of the active region, s and w the spacing and width of the fingers and α the absorption coefficient as a function of the wavelength.
For an ideal MSM photodetector the internal quantum efficiency, which is defined as the number of electron-hole pair generated per incoming photon and collected at the

electrodes, equals unity. However, if multiplication mechanisms are present, the number of collected carriers increases, and the internal quantum efficiency can be larger than 100 % and give rise to G_i. In case no gain is present, the theoretical responsivity is:

$$R \leq \frac{\lambda\eta}{1.24 \times 10^{-6}} \mathrm{A/W} \tag{2.43}$$

Due to the forbidden bandgap, the limiting wavelength for photoexcitation is: $\lambda \leq \frac{hc}{E_g}$.
In order to optimize the responsivity of a MSM photodetector, the different factors which contribute to the quantum efficiency will be discussed.
First, the wavelength dependence of the responsivity is significant since the photon wavelength determines the absorption of light into the semiconductor. The light passes through the device decreases exponentially according to $e^{-\alpha x}$, where x the distance measured from the surface of the semiconductor. Hence, the amount of absorbed light is determined by the factor $(1 - e^{-\alpha x})$. The penetration depth γ of light into GaN can be deduced from its absorption spectrum by $\gamma = 1/\alpha$. In figure 2.13, it can be seen that the absorption depends on the wavelength with a sudden increase at energies above the bandgap energy (3.39 eV for GaN at room temperature). From this figure, it can be derived that the penetration depth of light is approximately 100-200 nm in GaN.

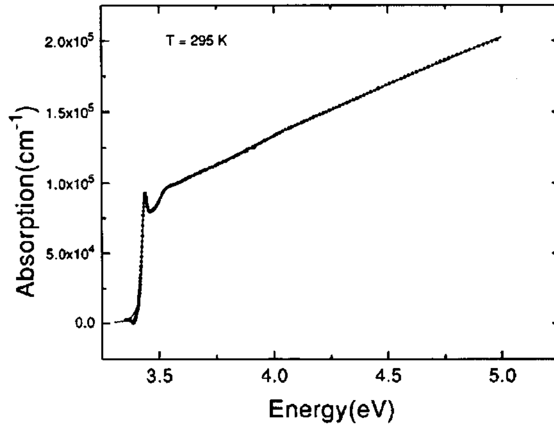

Figure 2.13: Absorption spectrum of GaN at room temperature

Secondly, in practice only a part of the incoming light reaches the active region of the photodetector. The reflection coefficient at the air-semiconductor interface for an incoming light coming perpendicular to the surface is:

$$r = \left(\frac{n_r(\lambda) - n_{air}}{n_r(\lambda) + n_{air}}\right)^2 \tag{2.44}$$

where $n_{air} = 1$ for air, and n_r the refractive index of the semiconductor. Between 200 nm and 365 nm, the reflection coefficient at the semiconductor/air-interface for GaN

is approximately constant and comes between 25 % and 28 %. In order to minimize reflection and thus improve sensitivity, an antireflection coating (ARC) can be used. Finally, the metal of the electrodes also affects the responsivity. In case of opaque electrodes, the fraction of light that will reach the semiconductor surface is the ratio of the finger spacing to the pitch: $(\frac{s}{s+w})$. If transparent electrodes are used, blocking of incoming light is reduced and more light is allowed to enter the active area.
As discussed, reflection and absorption in the Schottky metal reduce the photodetector responsivity. Due the transparency of (polished) sapphire, back illumination (illumination through the substrate) can reduce reflection losses. However, the carriers are photo-generated close to the semiconductor/substrate interface and must diffuse to the space-charge region before collection by the electrodes. Therefore, the responsivity decreases if the diffusion length of the carriers in not long enough. This is mostly the case because the semiconductor/substrate interface is an area with a large density of defects, which can act as recombination centers, due to the large lattice mismatch. Hence, front illumination through the Schottky metal is the only configuration which is preferable.

In MSM photodetectors, the photocurrent depends on the applied bias and on the light intensity. An observed property is that the photocurrent shows an initial increase followed by saturation and subsequent sharp increase before breakdown occurs. Figure 2.14 shows the potential profile on a n-type MSM device under low applied voltage and under illumination. The cathode is reverse biased by V_1, while the anode is forward biased by V_2. The total photocurrent is the sum of the photocurrents at the cathode and the anode on the semiconductor side.

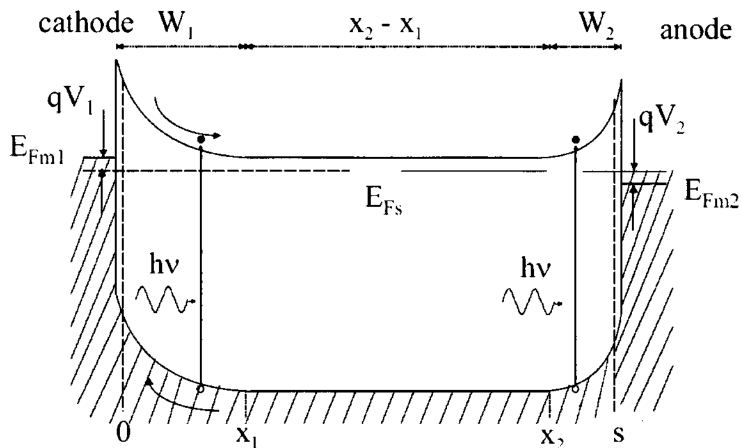

Figure 2.14: Energy band diagram of a MSM photodetector under low bias voltage and under illumination

The photocurrent density from the small voltage range $V < V_{RT}$ up to voltages larger than the reach-through voltage $V > V_{RT}$ is determined by [7]:

$$J_{ph} = -qG(W_1 - W_2) \tag{2.45}$$

where W_1 and W_2 are the depletion region width as defined in eqns. 2.27 and 2.28, and G the carrier generation rate (number of generated electron-hole pairs per time- and volume unit). Eqn. 2.45 is derived from the current continuity equation in the depletions regions assuming that carrier recombination can be neglected. It takes only the photo-generated electron-hole pairs which are generated in the depletion regions of the cathode and anode into account. This assumption is valid if we assume that the undepleted region is much larger than the diffusion length. At reach-through, the length of the undepleted region $x_2 - x_1 = 0$.

The light induced generation rate of electron-hole pairs as a function of distance x from the surface is $g(x) = \Phi_0 \alpha e^{-\alpha x}$, where $\Phi_0 = \frac{P_{opt}}{h\nu A}$ is the incoming photon flux per unit surface area and α the absorption coefficient of the semiconductor. Integrating the generation rate over the thickness of the active semiconductor region d and taking into account the internal quantum efficiency η_i gives:

$$G = \frac{1}{d}\int_0^d \frac{P_{opt}\eta_i}{h\nu A}\alpha e^{-\alpha x}dx = (1 - e^{-\alpha d})\frac{P_{opt}\eta_i}{h\nu A d} \tag{2.46}$$

At flatband, the depletion region of the cathode reaches the anode, making the electric field at the anode zero. For voltages larger than the flatband voltage, the photocurrent density per cross section area is characterized by:

$$J_{ph} = qGs \tag{2.47}$$

The photocurrent for a MSM structure in DC steady state under constant illumination, taking into account the surface reflectivity r, the shadowing due to the metal fingers and using eqns. 2.46 and 2.47, becomes:

$$I_{ph} = (\frac{s}{s+w})(1-r)(1 - e^{-\alpha d})\frac{qP_{opt}\eta_i}{h\nu} \tag{2.48}$$

In this equation, opaque electrodes are considered because the term $(\frac{s}{s+w})$ defines the fraction of the free semiconductor surface. Eqn. 2.48 is only valid when the voltage is above flatband voltage and therefore the current is saturated. In the other voltage regions, the total current characteristics can be modeled by combining the contributions of the photocurrent I_{ph} (eqn. 2.48) and the thermionic emission current density J_{dark}, which is described in section 2.3.3.[8]

2.4 Comparison of Schottky Barrier Diode and the P-N Junction Diode

Although the ideal current-voltage characteristic of the Schottky barrier diode given by eqn. 2.12 is of the same form of that of the p-n junction diode, there are two important differences between a Schottky diode and a p-n junction diode: the magnitude of the reverse-saturation current densities and the switching characteristics.

We will compare a Schottky diode made from a n-type semiconductor with a p-n junction having the same barrier height (see figure 2.15) [5].

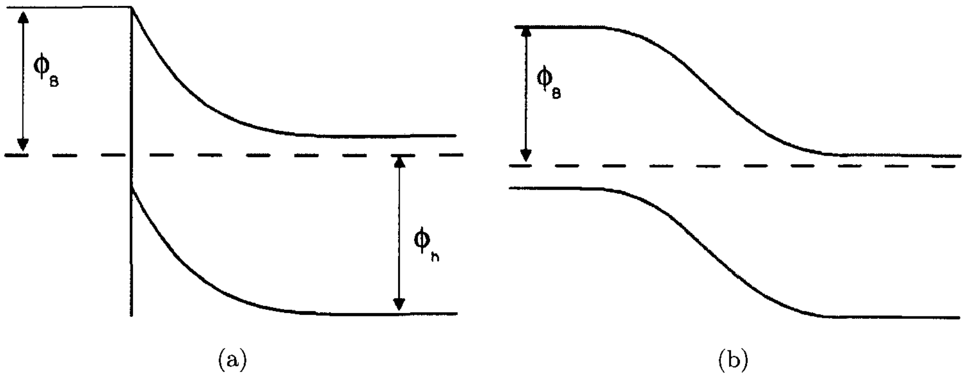

Figure 2.15: Band diagram of (a) Schottky barrier and (b) p-n junction showing the definition of ϕ_B and ϕ_h

The current mechanism in the two devices are different. The current in a p-n junction is determined by the diffusion of minority carriers while the current in a Schottky barrier diode is determined by thermionic emission of majority carriers over a potential barrier. To ensure that also the current in the p-n junction is carried almost by electrons, we will assume that the p side is slightly more doped than the n side.
Assuming that the current through the p-n junction is carried completely by electrons, the I-V characteristic is given by

$$J_{pn} = J_{spn}[\exp{(qV/k_BT)} - 1] \tag{2.49}$$

where

$$J_{spn} = \frac{qD_eN_c}{L_e}\exp{(-q\phi_B/k_BT)} \tag{2.50}$$

where D_e and L_e are the diffusion constant and diffusion length respectively of the electrons in the p-type side. Eqn. 2.50 can be rewritten using the relationship from kinetic theory that $D_e = \overline{v}l_e/3$, where l_e is the mean free path of electrons in the p region and $\overline{v}$ their mean thermal velocity. Moreover, $l_e = \overline{v}\tau_{ce}$ and $L_e = \sqrt{D_e\tau_{re}}$, where

τ_{ce} is the mean time between collisions and τ_{re} the lifetime of electrons in the p-type side. Then, Eqn. 2.50 becomes

$$J_{spn} = \frac{qN_c\overline{v}}{\sqrt{3r_e}} \exp\left(-q\phi_B/k_BT\right) \tag{2.51}$$

where

$$r_e = \frac{\tau_{re}}{\tau_{ce}} \tag{2.52}$$

For a Schottky diode the I-V characteristic is normally given by the thermionic emission theory according to

$$J_S = J_{sS}[\exp\left(qV/k_BT\right) - 1] \tag{2.53}$$

where

$$J_{sS} = \frac{qN_c\overline{v}}{4} \exp\left(-q\phi_B/k_BT\right) \tag{2.54}$$

Comparison of eqns. 2.51 and 2.54 gives

$$\frac{J_{sS}}{J_{spn}} = \frac{\sqrt{3r_e}}{4} \approx \sqrt{r_e} \tag{2.55}$$

For a GaN p-n junction, a typical value of τ_{re} is $\sim 10^{-9}$s [9] while $\tau_{ce} \sim 10^{-13}$s, and therefore $\sqrt{r_e} > 10^2$. Hence for the same barrier height the saturation current density of a Schottky diode exceeds that of a GaN p-n junction by a factor of 10^2 or more. For a long-lifetime semiconductor like Si, the ratio is larger and can be 10^3 or more.

In MSM structures, also the hole injection have to take into account if voltages larger than the reach-trough voltage are applied (see section 2.3.3). The injection of holes from the metal into the semiconductor is analogue to the injection of holes into the n-type side of the p-n junction. The transport of holes through the depletion region of a Schottky barrier and their subsequent diffusion in the neutral region of the semiconductor is identical to the mechanism of hole transport in a p-n junction. Therefore, we can write

$$J_h = J_{sh}[\exp\left(qV/k_BT\right) - 1] \tag{2.56}$$

where, by analogy with eqn. 2.51

$$J_{sh} = \frac{qN_v\overline{v}}{\sqrt{3\tau_h}} \exp\left(-q\phi_h/k_BT\right) \tag{2.57}$$

where ϕ_h the barrier for holes and $r_h = r_{rh}/r_{ch}$. The hole-injection ratio γ_h is therefore given by

$$\gamma_h = \frac{J_h}{J_h + J_e} \approx \frac{J_h}{J_e} = \frac{4N_v}{\sqrt{3r_h}N_c} \exp\left(-q(\phi_h - \phi_B)/k_BT\right) \tag{2.58}$$

or

$$\gamma_h \approx \frac{1}{\sqrt{r_h}} \exp\left(-q(\phi_h - \phi_B)/k_BT\right) \tag{2.59}$$

because J_e is the thermionic-emission current given by eqns. 2.53 and 2.54 and $N_c \approx N_v$.
This equation shows that γ_h increases with increasing ϕ_B because in that case J_e reduces and γ_h decreases with increasing ϕ_B because J_h reduces. For most Schottky barriers and certainly for GaN Schottky barrier diodes due to their large bandgap: $\phi_h > \phi_B$, so the exponent is negative. Hence, the hole injection ratio is generally small and therefore the Schottky barrier diode is a majority carrier device. However, due to the decreasing hole barrier with increasing voltage (voltages larger than the reach-through voltage) in MSM structures the hole current will also play an important role in these devices.

The second major difference between a Schottky barrier diode and a p-n junction is the frequency response or switching characteristics which are determined by the minority-carrier storage due to the minority-carrier injection. If the bias in a p-n junction diode is suddenly changed from forward to reverse, the electron and hole concentrations injected into the p side and n side respectively will start to decrease before the diode can retain a high-resistance state. This is in contrast with a Schottky barrier diode which is a majority carrier device. When switching a Schottky diode from forward to reverse bias, there is no minority carrier stored charge to remove. Since there is no minority carrier storage time, the Schottky diodes can be used in fast-switching applications.

Chapter 3

Results and Discussion

3.1 Fabrication of MSM and Schottky Barrier Photodetectors

The MSM and Schottky barrier photodetectors were fabricated on a quarter of a 2 inch GaN on sapphire wafer. The GaN layers were grown by metalorganic chemical vapor deposition (MOCVD) on sapphire substrates ($\pm$ 330 μm). Due to the high lattice mismatch between GaN and sapphire, first, a 25 nm low temperature buffer layer of GaN was deposited on the substrates. Then a thicker high-temperature GaN layer (2-3 μm) was grown, which was unintentionally doped to prepare MSM photodetectors. Nevertheless, the doping concentration in these wafers was still in the 10^{15} - 10^{16} cm^{-3} range. The cause of this unintentionally n-type (electrons) conductivity is still widely debated (see section 2.2.2). Otherwise, the GaN layers to prepare Schottky barrier photodetectors had a larger electron concentration (2.5×10^{17} cm^{-3}). This will ensure a good ohmic contact due to a thinner Schottky barrier and therefore the increase of the tunneling probability of the majority carriers through that Schottky barrier.

To fabricate MSM photodetectors (figure 3.1), a test mask was used with 6 different active areas (100×250, 100×100, 66×66, 50×50, 40×40 and 33×33 μm^2). The gap spacing (s) between the interdigitated electrodes and the finger width (w) was varied as well (0.5 ,1 ,2 ,4 and 8 μm). Two different electrode metallization, gold and platinum, were used to make MSM photodetectors. These metals are the most suitable ones because Au and Pt have high workfunctions, 5.10 eV and 5.65 eV respectively, and therefore a large barrier height can be achieved. The Au electrodes were deposited using radio-frequency (RF) sputtering in an argon plasma. The Pt contacts could only be deposited by electron-beam evaporation. Due to the evaporation of the Pt contacts (better surface contact when using sputtering) and the bad adhesion of the Pt to the GaN, a thin titanium layer was rf-sputtered to promote the adhesion. The MSM electrodes were then defined by standard photolithography and a lift-off process. With this lift-off process, only gap spacing larger than 4 μm can be obtained. Smaller

gap spacings were only achieved by using wet chemical etchants. Finally, the contact pads were formed by a lift-off process using a TiW/Au (10nm/160nm) metallization.

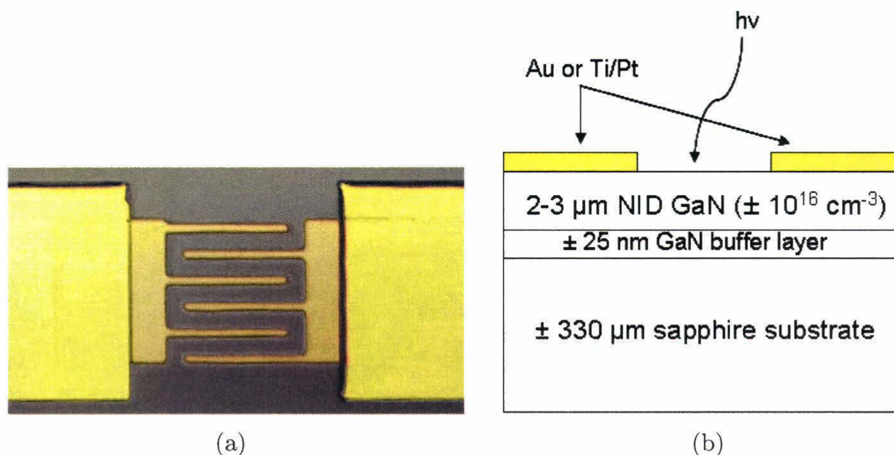

(a) (b)

Figure 3.1: (a) Microscope photo of a 8 μm gap spacing MSM photodetector (66 × 66 μm^2). (b) Cross-sectional view of the device shown in (a).

In this thesis, also lateral Schottky barrier photodetectors (figure 3.2) were fabricated for reasons discussed in detail in section 3.4. Therefore, a mask with rectangular shaped Schottky (90 × 290 μm^2) and ohmic contacts was used. First, the ohmic contacts were formed by using a lift-off process, using a Ti/Al/Mo/Au (20/40/25/50 nm) alloy which was annealed at 550 °C for 15 minutes and at 750 °C for 1 minute. This configuration has a very low contact resistance of ± 0.4 Ωmm. In this study, Schottky barrier photodetectors with Au, Ni, ITO and ITON Schottky contact metallizations were prepared. The 30 nm thick Au and Ni Schottky contacts were rf-sputtered in an argon plasma and defined by a lift-off process. The details of the ITO and ITON deposition techniques and properties will be discussed in detail in section 3.4.
The processing details to fabricate the MSM and Schottky barrier photodetectors with all the cleaning and photolithography procedures are summarized in Appendix A.

For a complete characterization of the MSM and Schottky barrier photodetectors, electrical (I-V, I-V-T and C-V) and optical (spectral responsivity, quantum efficiency and internal gain) measurements are performed.

The I-V and I-V-T characteristics of the photodetectors were measured using an Agilent 4156C semiconductor parameter analyzer and a Temptronic thermochuck (TP03215B) with a temperature range from 0 °C until 300 °C. In order to achieve low-noise measurement of the dark current, a Cascade Summit probing station was used. This probe station uses a shielded MicroChamber to eliminate electrostatic and electromagnetic interference to ensure a dark and noise-free measurement environment. With the Fem-

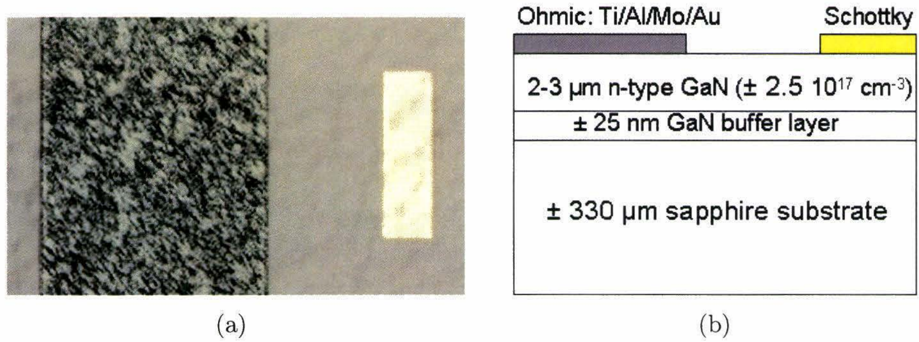

(a) (b)

Figure 3.2: (a) Microscope photo of a Ni Schottky barrier photodetector (90 × 290 μm^2). (b) Cross-sectional view of the device shown in (a).

toGuard chuck and the triaxial shielding probes down to the tip, accurately low current measurements down to ± 10 fA could be achieved. The C-V measurements were performed with a computer controlled Agilent 4284A Precision LCR meter on the same probing station.

The optical measurement were performed by using a 150 W Xenon arc lamp and a Sutter Lambda 10-2 optical filter wheel. In the optical set-up, 13 optical bandpass filters were installed from 200 nm until 400 nm (20 nm step). Also the bandpass filter for 370 nm and 390 nm were installed to characterize the cut-off wavelength accurately. The optical UV bandpass filters had a transmission band of ± 5 nm FWHM. The light that emerged from the filter wheel was coupled into one end of a UV enhanced fiber. The other end of the fiber was precisely positioned over the device under test. The optical system was calibrated using a SiC UV detector (IFW JEC 0.1 SS) with known absolute spectral response.

3.2 Dark Current Mechanisms in MSM Photodetectors

The aim of this section is to perform a detailed characterization and analysis of the dark current in MSM photodetectors and to identify all the conduction mechanisms which contribute to the dark current. In order to achieve this goal, a general description of the dark current will be made first and compared with the MSM theory. After that, the measured dark current will be compared and fitted with different current-transport mechanisms/models. In all these models, the barrier height and the Richardson constant are considered as known parameters. Due to the two Schottky barriers back-to-back by MSM photodetectors, the extraction of these parameters will give cause for some problems. These will be first solved by a detailed discussion and comparison of different techniques to extract the barrier height and Richardson constant as accurate as possible.

3.2.1 Global Description Dark Current

A detailed description of the MSM theory was already given in section 2.3.3. There, three operations regions were distinguished in function of the applied voltage:
The "low-current" region, corresponding to applied voltages smaller than the reach-through voltage. In this case, the MSM photodetector is not fully depleted and the current is mainly due to the transport of majority carriers.
The "injection" region, corresponding to applied voltages between the reach-through voltage and the flat-band voltage. In this region, the MSM photodetector is completely depleted of carriers, but the peak of the barrier for holes still lies within the semiconductor. The barrier height for holes is a decreasing function of the applied voltage and therefore, the hole current increases rapidly.
The "saturation" region, corresponding to applied voltages larger than the flat-band voltage. In that case, the barrier height for the holes lies at the semiconductor-metal interface and will only lower due to the image force and therefore, the hole current will be saturate.

In order to verify the presence of these 3 regions, MSM photodetectors (25 nm Au, s = w = 8 μm) are prepared. Figure 3.3 shows the plot of the I-V curve under dark condition for the MSM photodetector at 200 °C. Below that temperature, the dark current is in the fA range and therefore too small to be detected accurately by the measurement set-up.

It can be seen that instead of three regions, only the "saturation" region is present. From eqn. 2.36, we know that the flat-band band voltage is only a function of the electron concentration (N_d) in the n-type GaN and the gap spacing (s) between the electrodes. Due to the small donor concentration in not-intentionally-doped (NID) n-type GaN, the flat-band voltage can occur already at very small voltages. To achieve this, the donor concentration has to be lower than 5×10^{15} cm^{-3} when a gap spacing of 8 μm is assumed. To prove this, a C-V measurement is performed to check if the MSM device is completely depleted. Figure 3.4 shows the C-V characteristic of a MSM photodetector (area = 100×250 μm^2, s = 8 μm) under dark condition measured at a frequency of 1 MHz and an AC-signal amplitude of 10 mV.

When a MSM photodetector is completely depleted, the capacitance becomes independent of the applied voltage. In this case and with the assumption that there is no interfacial layer, the capacitance per unit area (C) is the same as that for a parallel plate condenser:

$$C = \frac{\epsilon_s}{s} \tag{3.1}$$

The value of the measured capacitance (0.105 pF) is in agreement with the value obtained from eqn. 3.1 (0.26 pF). The small difference in both values can be explained by an uncertainty in the MSM area.

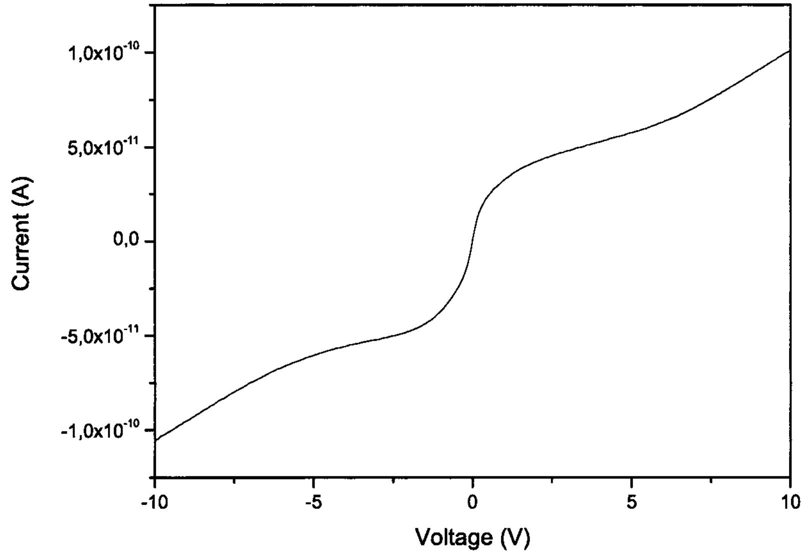

Figure 3.3: I-V characteristic of the MSM photodetector under dark condition

Hence, we can conclude that all our MSM devices are operating in the "saturation" region. In this region, the dark current is given by eqn. 2.40. To get an idea of the contribution of respectively the electron and hole current to the dark current, an estimation is made using this equation. We assume the theoretical Schottky barrier height for electrons of ± 1 eV when an Au metallization is prepared on GaN. Therefore the Schottky barrier for holes becomes E_g - 1 eV = ± 2.4 eV. In that case, the electron current is approximately 24 orders of magnitude larger than the hole current if the small influences of barrier height lowering and different Richardson constants are neglected. Hence due to the large bandgap of GaN, the dark current in GaN MSM photodetectors is approximately completely determined by the electron current. This is in contrast with for example GaAs MSM photodetectors, where the hole current dominates the "injection" and "saturation" region because the barrier height for the holes becomes smaller than for the electrons in these regions.

The "saturation" region is also the normal operation mode for MSM photodetectors because in this region, the photo-generated carriers will be swept to the electrodes at their saturation voltage due to the strong electrical field. Therefore as low as possible donor concentrations will be used in n-type GaN, not only to achieve a high quality Schottky barrier, but also to become full depletion of the MSM photodetector with reasonable gap spacing between the electrodes.
In figure 3.3 can be seen that the dark current rises slowly with the applied voltage and

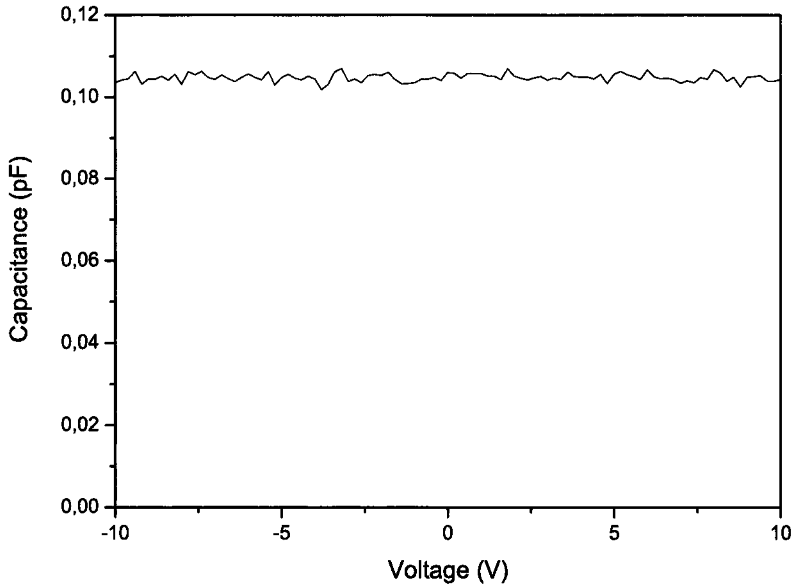

Figure 3.4: C-V characteristic of the MSM photodetector under dark condition

does not show any effect of saturation. The lack of saturation for a general Schottky contact under reverse bias can be commonly explained in terms of barrier lowering or the barrier height is dependent on the electrical field in the barrier as a result of the existence of an interfacial layer between the metal and the semiconductor. The lack of saturation can also be caused by image force lowering of the barrier height and due the generation of electron-hole pairs in the depletion region [5]. A detailed discussion of these mechanisms, especially applied on GaN MSM photodetectors, will be given in section 3.2.3.

Finally, we notice that in agreement with the MSM theory, the current is completely symmetric around 0 V if the same metallization and size is chosen for the anode and the cathode. Therefore, in the future only positive bias voltage will be applied to the MSM photodetectors without any loss of validity.

3.2.2 Schottky Parameter Determination in MSM Photodetectors

Due to two Schottky contacts back-to-back in MSM devices, the extraction of the Schottky parameters is not always obvious. When a voltage is applied, one of the Schottky contacts is forward and the other is reverse biased. Only the reverse I-V characteristics of these Schottky contacts can be measured. Therefore, in this section,

different techniques to extract the Schottky barrier height and the effective Richardson constant from I-V-T measurements will be presented and discussed in detail. The knowledge of these parameters is essential to understand and fit the dark current characteristic of MSM photodetectors. First, the effective Richardson constant will be determined because this constant is needed to extract the Schottky barrier height from the different measurements.

Effective Richardson Constant (A**)

The current-voltage characteristic according to the thermionic-emission theory for Schottky barrier diodes is given by:

$$I = AA^{*}T^{2}e^{\frac{-q\phi_B}{k_BT}}\left(e^{\frac{-qV}{nk_BT}} - 1\right) \tag{3.2}$$

where

$$A^{*} = \frac{4\pi m^{*} q k_B^2}{h^3} \tag{3.3}$$

where A^{*} is the Richardson constant for thermionic emission and only dependent of the semiconductor effective mass (m^{*}). For GaN, the theoretical Richardson constant for electrons is given by:

$$A^{*} = 120\left(\frac{m^{*}}{m}\right)\frac{A}{cm^2K^2} = 26.4\frac{A}{cm^2K^2} \tag{3.4}$$

The Richardson constant was introduced by Crowell and Sze [10] and represents the recombination velocity (V_r) at the top of the barrier. In terms of the thermionic-emission theory which assumes that no electrons which pass over the maximum of the potential barrier are scattered back into the semiconductor, $V_r = \bar{v}/4$ where $\bar{v}$ is the mean thermal velocity of electrons in the semiconductor. However, according to quantum mechanics, an electron may be reflected by a potential barrier even if it has sufficient energy to pass the barrier. The probability of an electron reaching the metal without being scattered back into the semiconductor is given by a factor f_p. Another effect is the quantum mechanical reflection and the tunneling of electrons through the top of the barrier. These two effects are combined by a factor f_q. Now, for the case in which thermionic-emission theory is valid, the effect of f_p and f_q is to replace A^{*} in eqn. 3.2 by $A^{**} = f_p f_q A^{*}$. In general, the effective Richardson constant A^{**} is less than A^{*}.

In order to determine the effective Richardson constant in the MSM photodetectors (25 nm Au), first, I-V measurements are performed at different temperatures. The result, where the temperature is varied between 200 °C and 300 °C, is shown in figure 3.5.

For $V \gg k_BT/q$, eqn. 3.2 can be written as [11]

$$\ln(I/AT^2) = \ln(A^{**}) - \frac{q(\phi_B - V/n)}{k_BT} \tag{3.5}$$

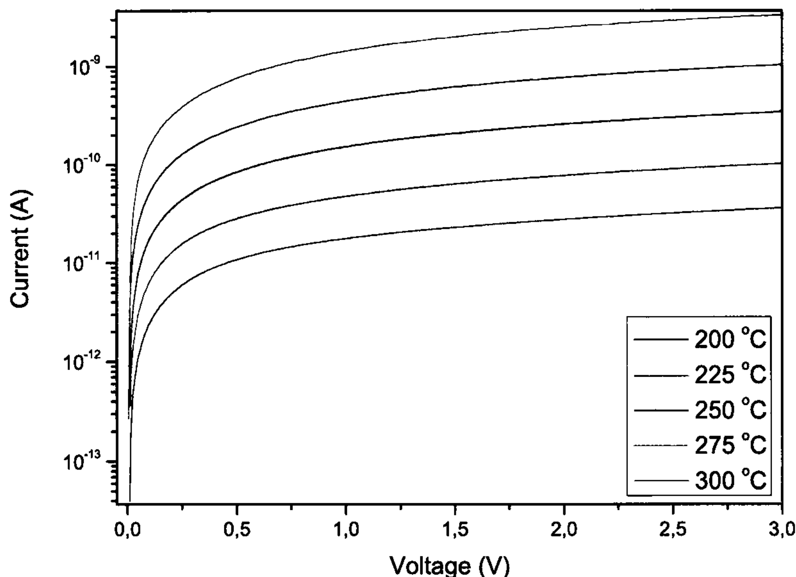

Figure 3.5: Temperature dependent I-V characteristic of the MSM photodetector under dark condition

To determine the effective Richardson constant, a plot of $\ln(I/AT^2)$ versus $1/T$ is made at a constant bias voltage $V = V_{bias}$. This Richardson plot has a slope of $-q(\phi_B - V_{bias}/n)/k_B$ and an intercept of $\ln(A^{**})$ on the vertical axis. The Richardson plot, extracted from figure 3.5 at a bias voltage of 0.2 V is shown in figure 3.6.

The y-intercept at this figure is at -1.28 $\pm$ 1.00. Therefore, the effective Richardson constant of the 25 nm Au MSM photodetectors is extracted to be 0.28 $\frac{A}{cm^2K^2}$. Theoretically, the Richardson constant is a property of the semiconductor because it is only dependent on the effective mass of the electrons. Therefore, the effective Richardson constant should be the same for all the MSM photodetectors on the same wafer and also for different metallizations. Nevertheless, Ti/Pt (5/25 nm) MSM photodetectors on the same wafer have a different effective Richardson constant (0.0045 $\frac{A}{cm^2K^2}$). The extracted effective Richardson constants in the MSM photodetectors are always two to four orders of magnitude lower than the theoretical ones. This is in agreement with literature [12], but to my knowledge never a detailed explanation is given.
First, the slope of the Richardson plot is well defined, but the extraction of the A^{**} from the intercept give cause to errors. Generally, the 1/T axis covers only a narrow range, 0.0017 to 0.0022 in our measurements. Extrapolating the data from that narrow range to 1/T = 0 involves extrapolating over a long range and any uncertainty in the

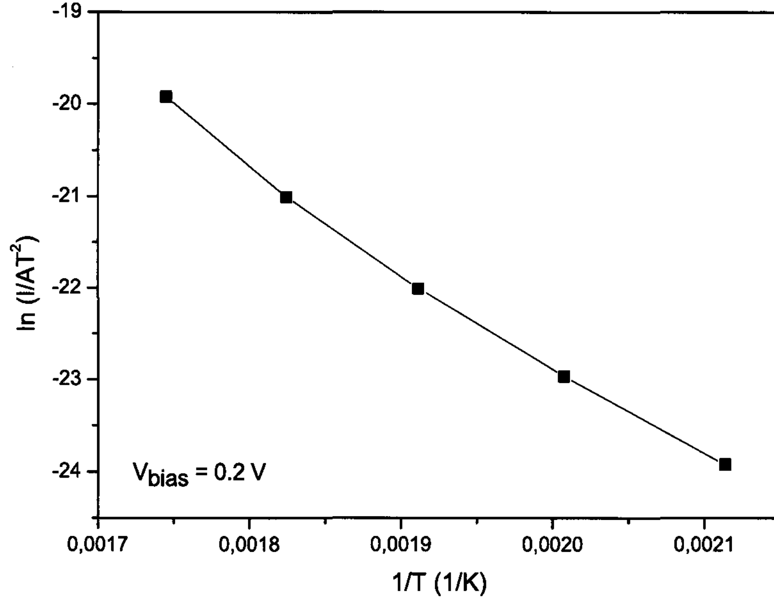

Figure 3.6: Richardson plot at 0.2 V of the MSM photodetector under dark condition

data produces a large uncertainty in A^{**}.
Secondly, to make a Richardson plot the current has to be divided by the MSM area which can be chosen on different ways. Because the whole MSM device is depleted, the whole active MSM area is chosen as junction area. This can give cause to a lower effective Richardson constant because the active area is the largest which can be chosen.
Finally, the extraction of the effective Richardson constant is done by supposing the thermionic-emission theory (see eqn. 3.5). Therefore, the obtained value will only be valid and accurate if the conduction mechanisms in the MSM photodetectors are also due to thermionic emission. Nevertheless, the low effective Richardson constant indicates already that tunneling currents play an important role. In that case, the probability factor f_q decreases and therefore lowers the effective Richardson constant. To estimate the error which is caused by using thermionic-emission theory to extract A^{**} in MSM photodetectors with tunneling currents, a simulation is performed using the thermionic-field emission theory (section 2.3.1) to obtain the I-V characteristics at different temperatures. The Richardson plot of this simulation (TFE, $\phi_B = 1$ eV, and $A^{**} = 26 \frac{A}{cm^2K^2}$) at 0.1 V bias voltage is shown in figure 3.7.

The obtained A^{**} from the Richardson plot is 3.37 $\frac{A}{cm^2K^2}$, which is approximately 10 times lower than the Richardson constant used in the simulation.

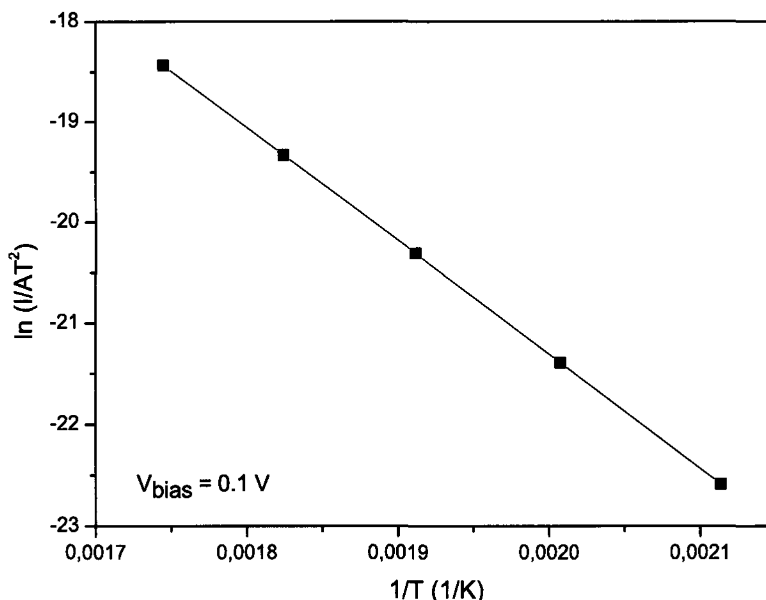

Figure 3.7: Richardson plot of the simulation using thermionic-field emission theory

Nevertheless, all these extrapolation errors could not explain completely the low effective Richardson constants. A physical interpretation of these low Richardson constants will be given in detail in section 3.4.

Schottky Barrier Height (ϕ_B)

The Schottky barrier height is most commonly calculated from the reverse saturation current (I_s), determined by an extrapolation of the ln(I) versus V plot to V = 0 V. The current axis intercept for the straight-line portion of this plot at V = 0 is given by I_s. The Schottky barrier height is calculated from (I_s) in eqn. 3.2 according to

$$\phi_B = \frac{k_B T}{q} \ln\left(\frac{AA^{**}T^2}{I_s}\right) \tag{3.6}$$

The ideality factor n can be extracted from the slope in this method and the Schottky barrier height is these for zero bias voltage.

This method is applied to 25 nm Au MSM photodetectors (Area: 100 × 250 μm^2, s = w= 8 μm) and the result which is measured at 200 °C is shown in figure 3.8.

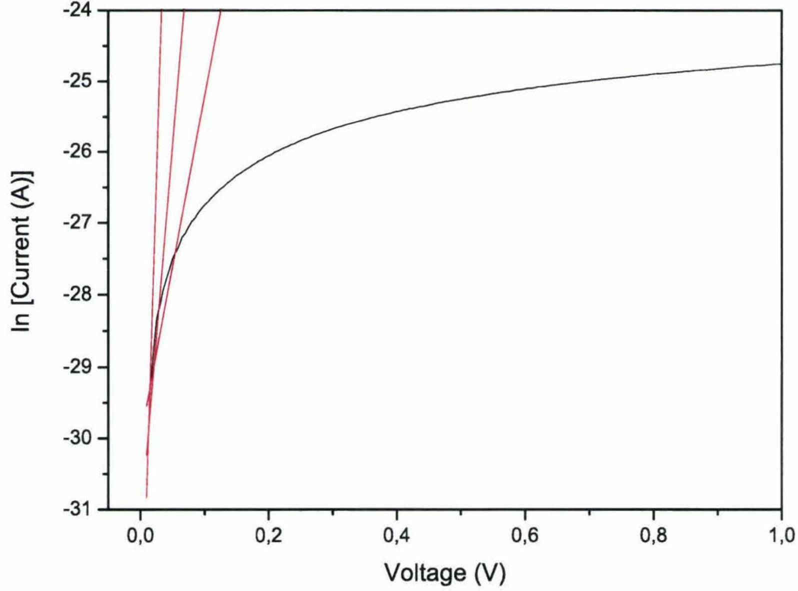

Figure 3.8: ln(I) versus V plot of a 25 nm Au MSM photodetector together with 3 possible extrapolations to extract the Schottky barrier height

In this figure, three suggestions are made to extract the reverse saturation current from the I-V characteristics. Like clearly shown on the graph, the voltage range where the value I_s has to be obtained is always very small in MSM photodetectors. Therefore, the number of data points which are taken into account for the extrapolation is crucial. Hence, this method is very user-dependent and will give cause to a large spread in the extracted Schottky barrier heights.
Averine *et al.* [13] worked out a new method to extract the Schottky parameters (ϕ_B and n) from the MSM I-V characteristics. They do not start from eqn. 3.2 to evaluate the Schottky parameters, but use the more general one which take into account a barrier height which is dependent on the applied voltage:

$$I = I_s \exp\left(\frac{qV}{nk_BT}\right)\left[1 - \exp\left(\frac{-qV}{k_BT}\right)\right] \tag{3.7}$$

A Schottky barrier height can be dependent on the electrical field due to image-force lowering or the presence of an interfacial layer [5]. The equation can also be written in the form of

$$\frac{I \exp\left(qV/k_BT\right)}{\exp\left(qV/k_BT\right) - 1} = I_s \exp\left(\frac{qV}{nk_BT}\right) \tag{3.8}$$

When V $\geq$ 0.5 V, eqn. 3.8 can be simplified to

$$I \exp\left(\frac{qV}{nk_BT}\right) = I_s \exp\left(\frac{qV}{nk_BT}\right) \tag{3.9}$$

$$\ln\left[I \exp\left(\frac{qV}{nk_BT}\right)\right] = \ln I_s + \frac{qV}{nk_BT} \tag{3.10}$$

The plot of $\ln(I \exp(qV/k_BT))$ versus V should give a straight line with slope = q/nk_BT and y-intercept at $\ln I_s$.

This method is also applied to 25 nm Au MSM photodetectors (Area: 100 $\times$ 250 μm^2, s = w = 8 μm) and the results which are measured at 200 °C, 250 °C and 300 °C are shown in figure 3.9.

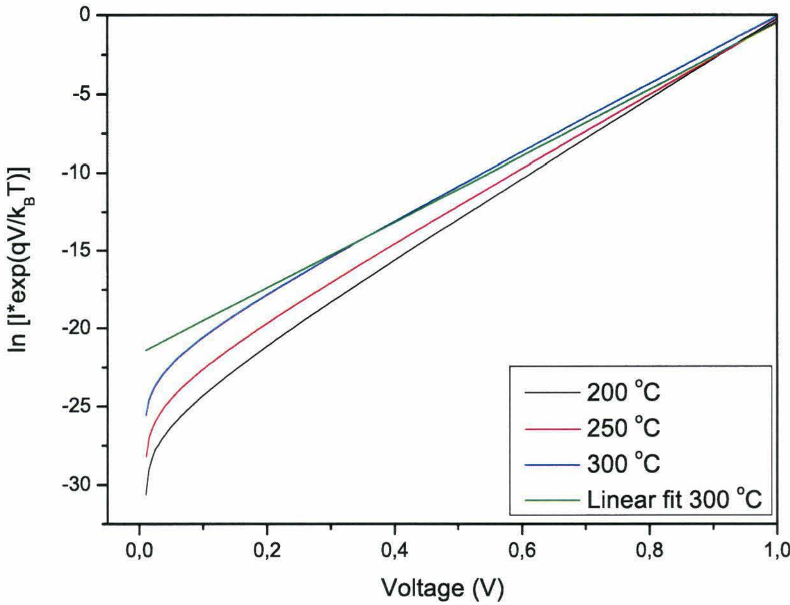

Figure 3.9: $\ln(I \exp(qV/k_BT))$ versus V plot of a 25 nm Au photodetector to extract the Schottky barrier height

Like shown in this figure, the reverse saturation current I_s increases with temperature like expected from the thermionic-emission theory. Using eqn. 3.6 and the calculated effective Richardson constant (0.28 $\frac{A}{cm^2K^2}$), the Schottky barrier height can be calculated from I_s. Because the value of A^{**} deviates much from the theoretical value, it is essential to use the calculated value to determine the Schottky barrier height. Nevertheless, at room temperature a 100 % increase in A^{**} results in a change of only

Temperature (°C)	200	250	300
ϕ_B (eV)	1.16	1.20	1.21
n	0.971	0.964	0.959

Table 3.1: Schottky barrier height (ϕ_B) and ideality factor (n) for 25 nm Au MSM photodetectors at different temperatures

10 meV to the Schottky barrier height. The value of the reverse saturation current is obtained from the y-intercept of a linear fit of the data points according to eqn. 3.10. An example of this linear fit is also shown in figure 3.9 for the I-V characteristic at 300 °C. The Schottky barrier height (ϕ_B) and ideality factor (n) for the MSM photodetector at different temperatures is given in table 3.1.

The value of I_s is completely determined by the I-V characteristic for applied voltage above 0.25 V, like shown in the linear fit in figure 3.9. According to eqn. 3.10, this method is only valid for voltages larger than 0.5 V. Nevertheless, when voltage larger than 0.5 V are applied to the MSM photodetectors, the current does not saturate when the reverse bias voltage increases. In this region, other conduction mechanisms are present and therefore this method is inadequate for GaN MSM photodetectors. This conclusion is also supported by the obtained ideality factor. With this method, ideality factors below 1 are found which is not possible by definition because the ideality factor (n) is given by [5]

$$\frac{1}{n} = 1 - \frac{\partial \phi_B}{\partial V} \tag{3.11}$$

or

$$n = 1 + \frac{\delta \varepsilon_s}{w(\delta q D_s + \varepsilon_i)} \tag{3.12}$$

where δ the thickness of the interfacial layer, ε_i the permittivity of the interfacial layer, w the width of the depletion region and D_s the density of the interface states. The effect of the bias dependence of the Schottky barrier height is to change the shape of the I-V characteristic by an increasing n-value when for example an interfacial layer or surface states are present. If the current does not saturate by using this method, the calculated slope (eqn. 3.10) is higher which results in a smaller n-value. Also the obtained zero-bias Schottky barrier height is too large compared with literature [14]. Theoretically, the Schottky barrier height for an Au contact on GaN will be 1.00 eV according to eqn. 2.1.

From this method, we can conclude that it is essential to know the reverse saturation current at very low voltages because the current does not saturate as expected by the MSM theory based on thermionic-emission. By using the first method, it was possible to extract the reverse saturation current at very small bias voltages. Nevertheless, the obtained Schottky barrier heights are showing a large scatter because the number of data points which are taken into account to fit and extract I_s is crucial.

Therefore, another method is needed to extract a reliable value of the barrier height at very small bias voltages.

The Norde method [15] which was originally derived to extract the barrier height from Schottky diodes with a high series resistance can be used to solve this problem. These method can also be applied to MSM photodetectors because the forward I-V characteristic of a Schottky diode with high series resistance "looks" similar to one of a MSM photodetector.
Using the Norde method, the Schottky barrier height can be obtained by plotting the $F(V) - V$ curve:

$$F(V) = \frac{V}{2} - \frac{k_B T}{q} \ln\left(\frac{I(V)}{AA^{**}T^2}\right) \tag{3.13}$$

where $I(V)$ originates from the measured I-V characteristic of the MSM photodetectors. From the minimum of the $F(V) - V$ curve, the Schottky barrier height can be expressed as

$$\phi_B = F(V_{min}) + \frac{V_{min}}{2} - \frac{k_B T}{q} \tag{3.14}$$

where $F(V_{min})$ the minimum point of the $F(V)$ curve and V_{min} the corresponding voltage.

This method is applied to 25 nm Au MSM photodetectors (Area: 100 $\times$ 250 μm^2, s = w = 8 μm) and the $F(V) - V$ curves which are measured at 200 °C, 250 °C and 300 °C are shown in figure 3.10.
From the $F(V) - V$ curves, it can be seen that the minima occur already at very low applied voltages. In this voltage region, the current increases a few orders of magnitude and saturates on a logarithmic scale at higher bias voltages. Therefore, the Norde method "thinks" that the saturation part is caused by series resistance and extract the Schottky barrier height at bias voltages around 0.1 V (see figure 3.10).
Hence, this method meets the conditions to determine reliable the Schottky barrier height of MSM photodetectors. The obtained barrier heights using the Norde method are summarized in table 3.2. It can be seen that ϕ_B is much smaller than using the previous method due to the more accurate and reliable determination of the reverse saturation current I_s. The values are also in agreement with other studies [14].

Temperature (°C)	200	250	300
ϕ_B (eV)	0.92	0.91	0.88

Table 3.2: Schottky barrier height (ϕ_B) for 25 nm Au MSM photodetectors at different temperatures using the Norde method

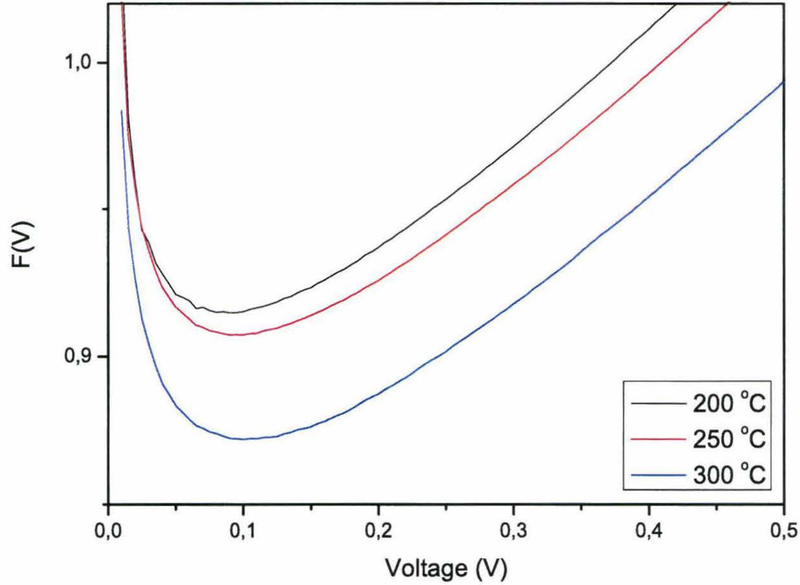

Figure 3.10: The F(V)-V curves of 25 nm Au MSM photodetectors at different temperatures

3.2.3 Modelling of the Dark Current Mechanisms

So far, the general I-V characteristics of MSM photodetectors are discussed and reliable techniques to determine the effective Richardson constant and the Schottky barrier height are presented.
A MSM photodetector consists of two back-to-back Schottky contacts: one forward biased and the other reverse biased. Due to the wide bandgap in GaN semiconductors, the hole barrier is much higher compared to the electron barrier. Therefore the current from the reverse-biased contact will account approximately for the entire behavior which is essentially the same as a Schottky diode with the forward-biased contact replaced by an ohmic, non-injecting contact. Therefore, to model the dark current mechanisms in MSM photodetectors the standard Schottky theory can be used together with the obtained effective Richardson constants and Schottky barrier heights by using techniques presented in section 3.2.2.

To model the dark current mechanisms, Ti/Pt (5/25 nm) MSM photodetectors (Area: 100×250 μm^2, s = w = 8 μm) are fabricated on NID GaN ($N_d = \pm 10^{16}$ cm^{-3}). The extracted effective Richardson constant and Schottky barrier height are 0.0029 $\frac{A}{cm^2 K^2}$ and 1.01 eV respectively for these MSM photodetectors.
In section 2.3.3, the theoretical dark current mechanisms of MSM photodetectors

are discussed. In the "saturation" region, the current is completely described by thermionic-emission theory with the Schottky barrier lowering effect. In figure 3.11, the I-V characteristic of a Ti/Pt MSM photodetector measured at 233 °C is shown together with a theoretical fit (see Appendix B) to the experimental data using this theory.

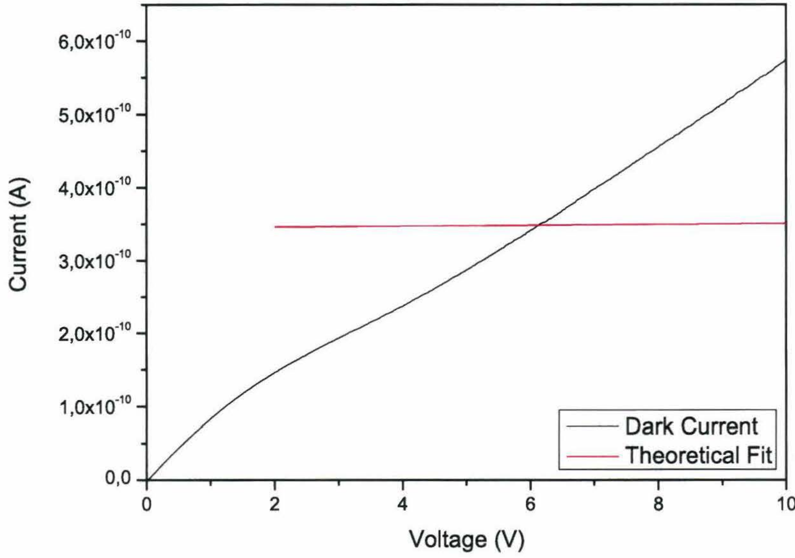

Figure 3.11: Dark I-V characteristic of a Ti/Pt MSM photodetector (black line) and theoretical fit using thermionic-emission theory with barrier lowering (red line)

It can be clearly seen that this theory can not fully explain the conduction mechanisms in the MSM photodetectors.
Another current transport mechanism which dominates in general the dark current in semiconductor photodetectors is the generation-recombination current density (J_{gr}) in the space-charge region according to eqn. 3.15:

$$J_{gr} = \frac{qn_i}{\tau}\sqrt{\frac{2\epsilon_s}{qN_d}(V_{bi} - V)}(e^{qV/2k_BT} - 1) \tag{3.15}$$

where τ the lifetime within the depletion region and n_i the intrinsic concentration given by:

$$n_i = \sqrt{N_c N_v} e^{\frac{-E_g}{2k_BT}} \tag{3.16}$$

where N_c and N_v the effective density of states in the conduction band and valence band respectively. However, for a wide bandgap semiconductor such as GaN, the intrinsic carrier concentration is very small at room temperature ($n_i = 4,5 \times 10^{-11}$ cm^{-3}).

According to eqn. 3.15, the contribution of the generation-recombination current to the total current can be estimated. In GaN MSM photodetectors, I_{gr} is approximately 10^{-20} A and therefore we can conclude that the generation-recombination current gives not a serious contribution to the dark current.

The lack of saturation suggests that an important tunneling component exists in the dark current of the MSM photodetectors. To model and fit the tunneling current through the Schottky barrier, the thermionic field emission (TFE) theory is used which is discussed in detail in section 2.3.1. In the TFE theory, the reverse current transport is due to electrons which are thermally excited from the metal Fermi level and tunnel through the semiconductor depletion region to the semiconductor conduction band. Because the MSM photodetectors are measured between 200 °C and 300 °C, only TFE will play an important role in the current transport mechanisms. Field emission (FE) will contribute only to the dark current if the temperature is lowered so that tunneling can only take place around the Fermi level. In figure 3.12, the result of the fit according to the TFE theory (see Appendix B) is shown.

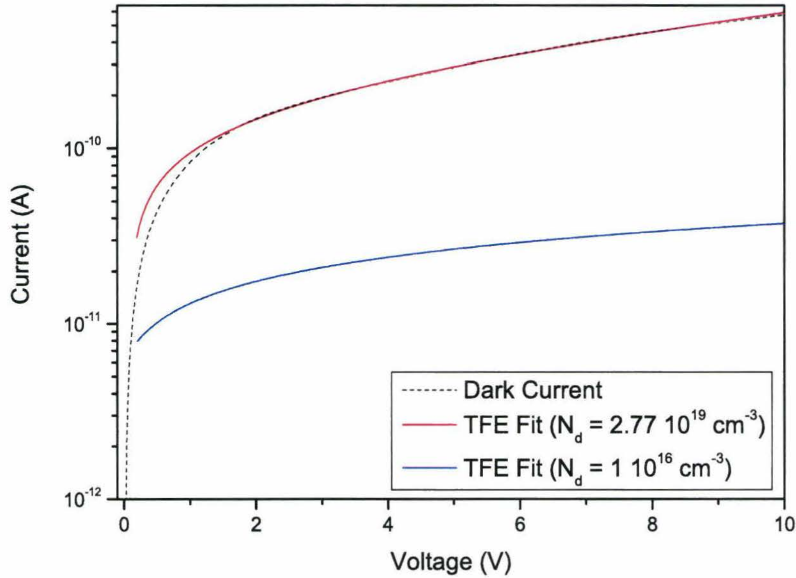

Figure 3.12: Dark I-V characteristic of a Ti/Pt MSM photodetector (dashed black line) and theoretical fit using thermionic field emission theory with $N_d = 2.77 \times 10^{19}$ cm^{-3} (red line) and $N_d = 1 \times 10^{16}$ cm^{-3} (blue line)

If an electron donor concentration (N_d) of 2.77×10^{19} cm^{-3} is assumed in the curve fitting using the TFE theory, the measured I-V characteristic agrees very well with

the theoretical curves as seen in figure 3.12. However, this value of N_d is far too large compared to the value of NID GaN and can not interpreted as possible fluctuations of the bulk donor concentration. To show the influence of the donor concentration of the I-V characteristics in the TFE theory, also the theoretical curve for a lower N_d and typical for our NID GaN is visible in the figure. In that case, the dark current is approximately one order of magnitude lower than the measured values and also the slope is too small. Hence, the TFE theory can also not explain the measured I-V characteristics of the MSM photodetectors quantitatively.

So far, numerous researchers have tried to explain the current transport mechanisms which are responsible for the large leakage current in GaN Schottky barrier diodes.
Sawada *et al.* suppose that the present leakage current seems due to non-uniform distribution of the Schottky barrier height, namely, existence of "surface patches" with lower values of the barrier height. In that case, the total current is given by the sum of currents passing through an usual high Schottky barrier region and patches with lower barrier heights [16]. Most probably, the origin of these patches are (surface) crystal defects and in particular threading dislocation with a screw component. These dislocations are found to be accompanied by high current densities and low effective Schottky barrier heights [17]. Typically, GaN layers have a large dislocation density ($\pm 10^9$ cm^{-2}) where most of them have a screw component.
Sawada *et al.* use this theory to model the forward current in GaN Schottky barrier diodes. Nevertheless, this theory can not explain the observed I-V characteristics in our MSM photodetectors. The "surface patches" could give an explanation for the larger dark current compared to the thermionic-emission theory with only one Schottky barrier height, but can not explain the lack of saturation because the theory of Sawada *et al.* uses also thermionic-emission.

Carrano *et al.* believe that the dark current can be modeled by assuming trap-assisted tunneling at the reverse-biased Schottky barrier. In that case, presence of discrete deep-level states or a continuum of trap states within the Schottky barrier is assumed, and they are supposed to provide tunneling paths through the energy barrier after capture of electrons by thermal excitation [18]. The traps are a combination of interface states and deep-level bulk states. The deep-level interface states are likely to be a combination of states associated with the contamination layer, the thin native oxide and threading dislocations. This trap-assisted tunneling model is shown schematically in figure 3.13.

We believe that trap-assisted tunneling can explain some of the I-V characteristics of our MSM photodetectors. The dark currents of a 25 nm Au MSM photodetector (Area: 100×250 μm^2, s = 8 μm, w = 2 μm) measured at room temperature are shown in figure 3.14.
The initial dark current is typical for this size of MSM photodetectors. However, after a second measurement of the dark current a significant degradation of the curve occurs. Afterwards, a I-V measurement is performed where the MSM photodetector

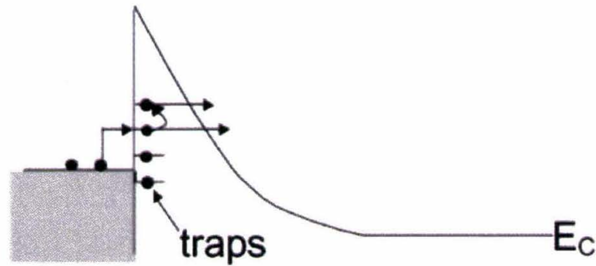

Figure 3.13: Trap-assisted tunneling as dark current mechanism

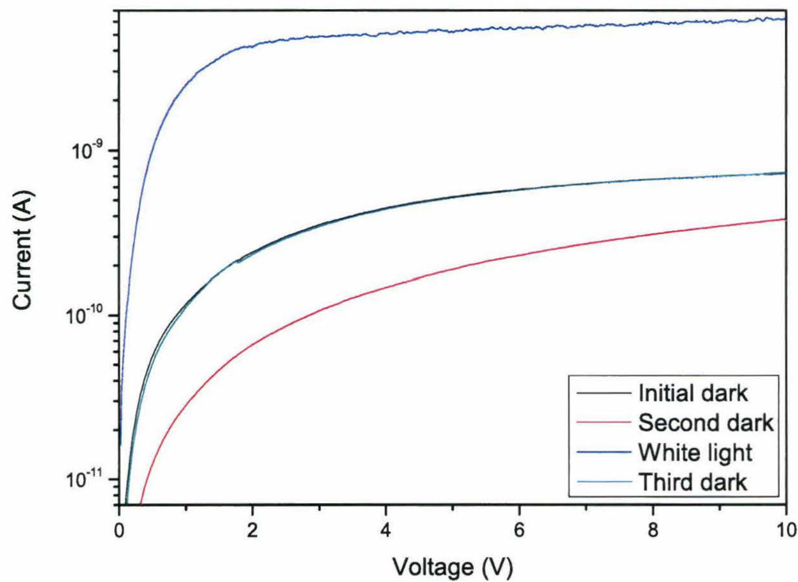

Figure 3.14: A set of dark currents of a MSM photodetector showing the degradation mechanism related to trap-assisted tunneling

is illuminated with the white light of the microscope. A dark current measurement taken subsequent to this white light illumination gives again a I-V characteristic that is equal to the initial dark current.

We believe that traps play an important role in the reported dark current characteristics. After an initial dark current measurement, deep level states become filled with trapped electrons that have tunneled from the metal into the semiconductor. After this measurement, most of the states will be filled and therefore a subsequent dark current measurement shows a degraded curve because there are less empty states to support

the trap-assisted tunneling process. White light illumination can cause de-trapping of the interface and bulk states due to the visible and IR light components. These photons with short wavelengths will strongly interact with the traps which are lying in the bandgap of the semiconductor. This is consistent with the observations of Binari *et al.* who concluded that illumination or heating depopulates traps in their GaN-based field effect transistors [19]. Therefore, a dark current measurement taken subsequent to the white light measurement will appear similar to the initial one because a larger number of states are available again to support the trap-assisted tunneling process.

Nevertheless, it is obviously difficult to model and fit the reported dark current by trap-assisted tunneling because it is a two step process. First, the carriers have to be captured by the trap states and afterwards they have to tunnel through the Schottky barrier. When carriers are captured by the trap or interface states, the charge neutrality at the junction will be disturbed. In presence of these traps, the neutrality condition becomes $Q_m + Q_d + Q_t = 0$, where Q_m the negative charge on the metal, Q_d the positive charge due to the ionized donor atoms and Q_t the charge in the trap states. Depending on the net positive or negative charge in the trap states, Q_d must therefore be smaller of larger respectively than if trap states were absent. This means that the depletion width will be correspondingly reduced or enlarged respectively. This mechanism will also play a important role in the current transport characteristics.
Nevertheless, measurements at low temperature could also lead to a better understanding of this process because the thermal excitation process of electrons to higher traps would be suppressed at these temperatures. Also the reliable Schottky parameter extraction from these MSM photodetectors is not possible because the measured dark current depends on the number of voltage sweeps.
Finally, it is important to notice that only MSM photodetectors on one GaN wafer show these reported dark currents characteristics. On other GaN wafers, the MSM dark currents do not suffer from this hysteresis. From that, we can conclude that the current transport mechanisms are much dependent on the "quality" of the GaN layer. A low dislocation density is one of the most critical parameters to achieve good quality GaN layers.

We believe that the measured dark currents without hysteresis can be explained by the thin surface barrier (TSB) model introduced by Hasegawa *et al.* [20]. This model is schematically shown in figure 3.15. This model assumes the formation of high densities of unintentional defect donors near the surface. This will reduce the width of the Schottky barrier and thereby enhance the electron tunneling through the Schottky barrier in both forward and reverse directions. In our case, thermionic field-emission as tunneling mechanism will be dominant due to the intermediate doping concentrations, low bias voltages and the high temperature (I-V characteristics measured between 200 °C and 300 °C).
In this model, they assume a rectangular distribution of defect donors on top of the uniform bulk doping. Therefore, the TSB region is characterized by a net surface donor concentration of N_{DS}, the thickness D and the ratio of the total TSB area to the total

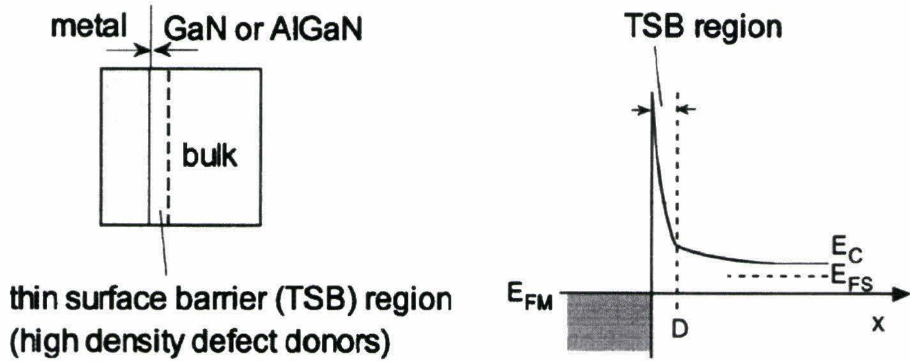

Figure 3.15: Schematic illustration and band diagram of the TSB model as dark current mechanism

sample area (η). Due to the high nonuniformity of the GaN surface involving many dislocation, it is likely that the TSB regions are distributed spatially nonuniformly. Assuming the rectangular distribution of defect donors, a set of analytical formulas are derived to fit the measured I-V characteristics [20].

In order to compare the TSB model with the I-V measurements of our MSM photodetectors, Ti/Pt (5/25 nm) MSM photodetectors (Area: 100 $\times$ 250 μm^2, s = w = 8 μm) are prepared and measured between 200 °C and 300 °C. The result of the measured dark currents together with the fitted curves using the TSB model (see Appendix B) are shown in figure 3.16.

According to the TSB model, the best fitting is obtained by assuming a defect donor concentration of 5 $\times 10^{18}$ cm^{-3} and a TSB region thickness of 3.05 nm. Because no information is available on the value of η, it is assumed to be one. In figure 3.16, the dark currents of the MSM photodetectors measured at different temperatures are all fitted with the same TSB parameters and the results are already satisfactory. To agree completely with the measured dark current, the TSB parameters have not to be changed much at different measurement temperatures, ranging from 2 $\times 10^{18}$ cm^{-3} to 7 $\times 10^{18}$ cm^{-3} for the defect donor concentration and from 2.5 nm to 5 nm for the TSB region thickness. Discrepancy takes only place at low bias voltage, where the current is extremely sensitive to the shape of the barrier because the TFE process takes place near the bottom of the barrier. During the fitting process, it became clear that the choice of the TSB parameters was very critical. To show this, the parameters sensivities to the reverse currents are plotted versus values of N_{DS} and D in figure 3.17 for various temperatures.
According to this figure, the TSB model predicts a very strong dependence of the I-V-T behavior on the TSB parameters. Therefore, it is essential to know the origin of these defect donors which from the TSB regions. According to Hasegawa *et al.*, they propose that defect donors are caused by nitrogen vacancies (V_N) or oxygen in

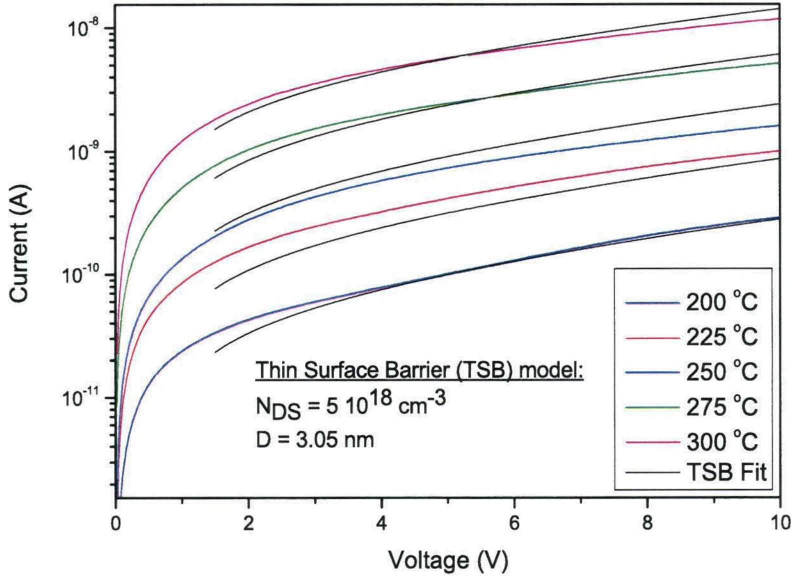

Figure 3.16: Dark I-V characteristics of a Ti/Pt MSM photodetector at different temperatures and theoretical fit using thin surface barrier model with $N_{DS} = 5 \times 10^{18}$ cm^{-3} and $D = 3.05$ nm (black lines)

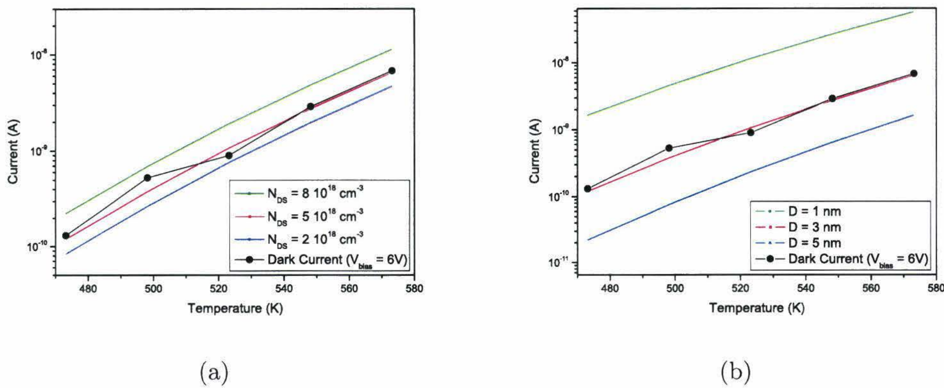

Figure 3.17: Calculated parameter sensivities of MSM dark current against the defect donor concentration N_{DS} (a) and the TSB region thickness D (b)

the nitrogen site (O_N). Also Neuenbauer and Van de Walle [3] have found indications by first-principle calculations that a N vacancy defect acts as a (shallow) donor. As

the formation mechanism of defect donors, they propose that the defect donors are introduced during the metal deposition by E-beam deposition or sputter deposition where the surface is hit by high-energy metal atoms. Also the presence of Ga atoms at the surface (Ga-face polarity) can possible play a role in the formation of TSB regions.

3.3 Photocurrent Mechanisms in MSM Photodetectors

The aim of this section is to perform a detailed analysis of the photocurrent in MSM photodetectors. To achieve this, a general description of the photocurrent will be made and compared with the dark current. Also the physical photocurrent mechanisms will be discussed in detail. The aim of MSM photodetectors is to detect only photons with larger energies than the bandgap. Therefore, a spectral response of the GaN MSM photodetectors will be made to verify if the photodetector is visible-blind. Finally, the quantum efficiency (QE) will be determined to characterize the optical performance of the MSM photodetectors.

In figure 3.18, a comparison between the dark current and the photocurrent of a 25 nm Au MSM photodetector (Area: 100 $\times$ 250 μm^2, s = w = 8 μm) is shown.

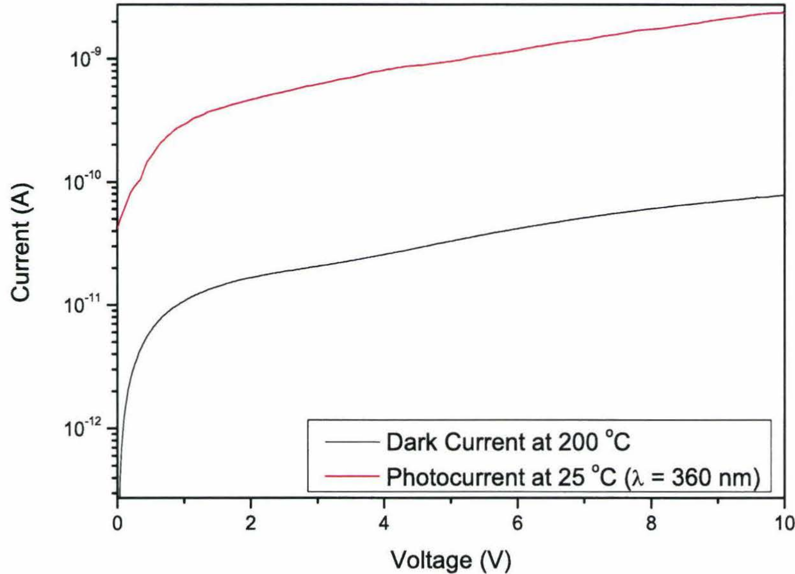

Figure 3.18: Comparison between the dark current and the photocurrent (λ = 360 nm) of a 25 nm Au photodetector

We remark that the dark current is measured at 200 °C because below that temperature the current is too low to perform the measurement accurately. Nevertheless, an estimation of the photocurrent to dark current ratio can be made. Assuming that the dark current at room temperature will be in the fA range, the signal-to-noise ratio is approximately 10^5 when the illumination power is approximately 25 nW at a wavelength of 360 nm.

In section 3.2.3, the dark current mechanisms are discussed in detail for MSM photodetectors. To examine if the same current transport mechanisms are responsible for the photocurrent, the I-V-T characteristics of the dark current and photocurrent are compared. These measurements are shown in figure 3.19 for 25 nm Au MSM photodetectors (Area: 100×250 μm^2, s = w = 8 μm) where the temperatures is varied between 200 °C and 300 °C.

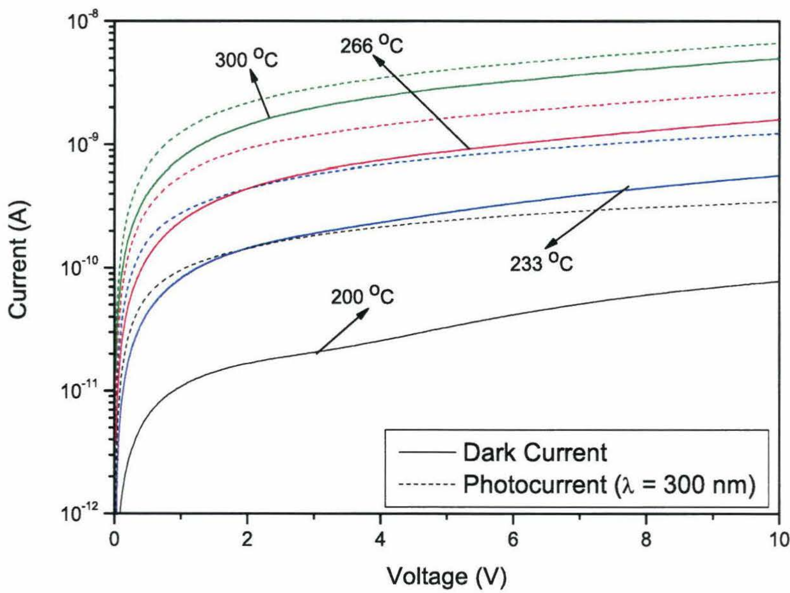

Figure 3.19: Dark current (solid lines) and photocurrent (dashed lines) I-V-T characteristics of 25 nm Au MSM photodetectors

It can be clearly seen on this figure that if the temperature is increased, the difference between the dark current and photocurrent becomes smaller. However, if the thermionic emission theory is also suitable for the photo current transport mechanisms (discussed in section 2.3.4), the difference between the dark current and the photocurrent has to be equal at all temperatures. This indicates that another conduction mechanism is responsible for the photocurrent. Therefore, we will calculate the

activation energy (E_A)/Schottky barrier height for both the dark and photo-current and the Arrhenius plot is shown in figure 3.20 when a voltage of 2 V is applied.

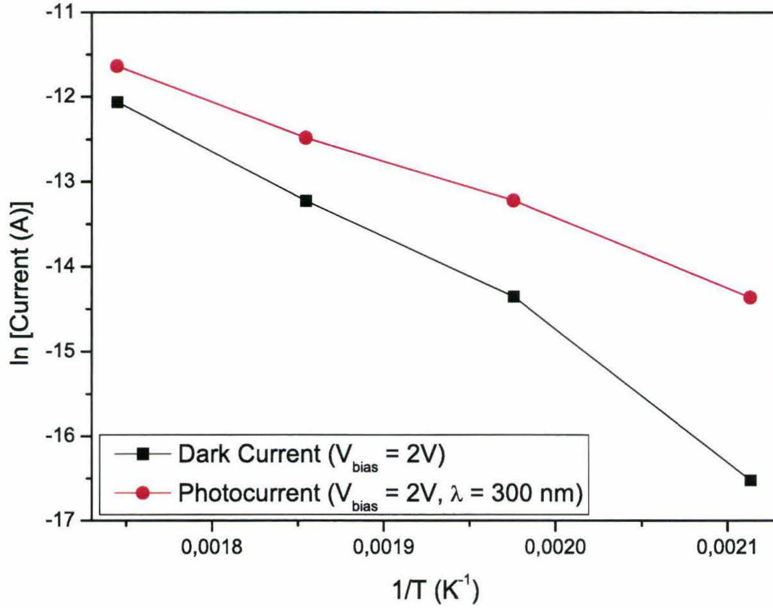

Figure 3.20: Arrhenius plot of the dark current and photocurrent of 25 nm Au MSM photodetectors

From the slope of the Arrhenius plot, the activation energy for the dark current (1.02 $\pm$ 0.09 eV) and the photocurrent (0.62 $\pm$ 0.02 eV) are calculated. We believe that if the MSM photodetectors are illuminated with UV light, the decrease of the activation energy can be caused by 2 mechanism.

Most probably, the Schottky barrier height is decreased due to a photo-generated charge carriers at the metal-semiconductor interface. The surface states (UV light penetration is around 100 nm) at the interface can trap the photo-generated carriers. If this happens, the charge neutrality condition at the interface becomes disturbed. To satisfy the junction neutrality condition again, the width of the depletion region has to be reduced. This means that the amount of band bending or the built-in voltage has to be reduced. This reduction under UV illumination will decrease the Schottky barrier height.

Another possible photocurrent conduction mechanism is based on trap-assisted tunneling. The traps are attributed to dislocations for example threading edge dislocations, having an donor-like nature with mid-gap energy [21]. The calculated activation energy is also approximately mid-gap, where also the (TFE) tunneling has the largest probability due to an optimum between the Schottky barrier thickness and the available

electrons. However, we believe that this mechanism is not responsible for photocurrent transport because it also could not explain the dark current in our MSM photodetectors without hysteresis effects.
In order to figure out which mechanism is responsible for the photocurrent, C-V measurements has to be made while the MSM photodetectors are UV illuminated. Then the variation of the Schottky barrier height can be clearly examined. Because the capacitance in our MSM photodetectors is constant, Schottky barrier diodes will be made. The results of these measurements will be discussed in section 3.4.

One of the most important parameters to describe the performance of a MSM photodetector is the responsivity (R). This is the ratio of the generated photocurrent to the incoming illumination with an optical power corresponding to a photon energy $h\nu$ at the wavelength λ:

$$R = \frac{I_{ph}}{P_{opt}} = \frac{\lambda \eta G_i}{1.24 \times 10^{-6}} \left(\frac{A}{W} \right) \tag{3.17}$$

where η the quantum efficiency of the device and G_i the internal gain.
The measured spectral response at room temperature for 25 nm Au MSM photodetectors (Area: $100 \times 250\ \mu m^2$, s = w = 8 μm) when a voltage of 8V is applied can be seen in figure 3.21. Also the quantum efficiency is calculated using eqn. 3.17 and plotted for each wavelength on the same figure.

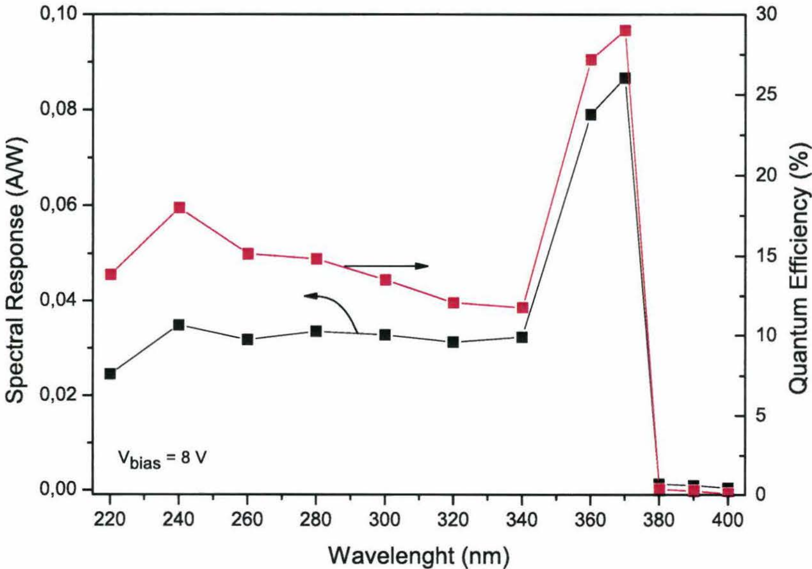

Figure 3.21: Responsivity of a 25 nm Au MSM photodetector as a function of wavelength (black dots) together with the calculated quantum efficiency (red dots)

On the figure, it can be clearly seen that the cut-off wavelength is situated around 370 nm. This is in agreement with the theoretically expected cut-off wavelength of 365 nm (bandgap GaN = 3.4 eV) if we also take into account the 5 nm FWHM of the UV band filters. There is also a sharp, visible-blind cutoff of more than 3 orders of magnitude at the band edge and below the bandgap there appears no considerable response.
At the band-edge, a significant peaking of the spectral response can be observed. This can be attributed to the existence of excitons (bounded electron-hole pairs) which are particulary important in GaN because the large binding energy permits them to still exist at room temperature. The wurtzite crystal structure with three valence bands allows three excitation transitions that are relative close together in energy. At room temperature, an exciton binding energy between 23,5 meV and 30 meV is determined [22]. Therefore, we can conclude that the photocurrent in this part of the spectral response is primarily attributed to excitons.
Below 340 nm, the responsivity is approximately constant at 0.03 A/W. We remark that the spot diameter of the incident UV light was larger than the MSM area, which is not optimal because carrier diffusion from the surroundings may influence the detected photocurrent. Assuming no gain mechanism is present in our MSM photodetectors, this responsivity equals to a quantum efficiency of approximately 15 %.

However, by measuring the responsivity of a function of the applied bias, we can obtain insight into the existence of an internal gain mechanism. The result of this measurement are shown in figure 3.22. Our MSM photodetectors show a linear dependence of responsivity on bias. Such a linear relationship is indicative of a photoconductive gain mechanism. This can be understood if following equations are considered [23]:

$$G = \frac{\tau}{\tau_{tr}^{e}} = \frac{\tau \mu_e V}{s^2} \tag{3.18}$$

where μ_e the electron mobility, τ the recombination lifetime, τ_{tr}^{e} the electron transit time, s the electrode gap spacing and V the applied voltage. As voltage increases the electron transit time decreases and the gain subsequently increases linearly. Generally, these equations are derived for photoconductors. In our case, the photocurrent does not saturate like expected from the theory in this voltage region (8V - 14V) which is shown in figure 3.18. We believe that this is caused by the traps at the metal-semiconductor interface like already mentioned. In that case, the traps are filled with photo-generated carriers and cause an increase in conductivity and hence photoconductive gain by subsequent re-emission. Therefore, we can conclude that following equation is more applicable for our MSM photodetectors:

$$I_{ph} \sim \frac{2 q n_{trap} \mu_e V}{s^2} \tag{3.19}$$

where n_{trap} is the number of trapped carriers. This equation assumes that the photocurrent is not limited by the recombination time but is proportional to the trapped photo-generated carriers. We believe that traps capture photo-generated charge carriers which causes the sweep-out and reinjection of other charge carriers to maintain

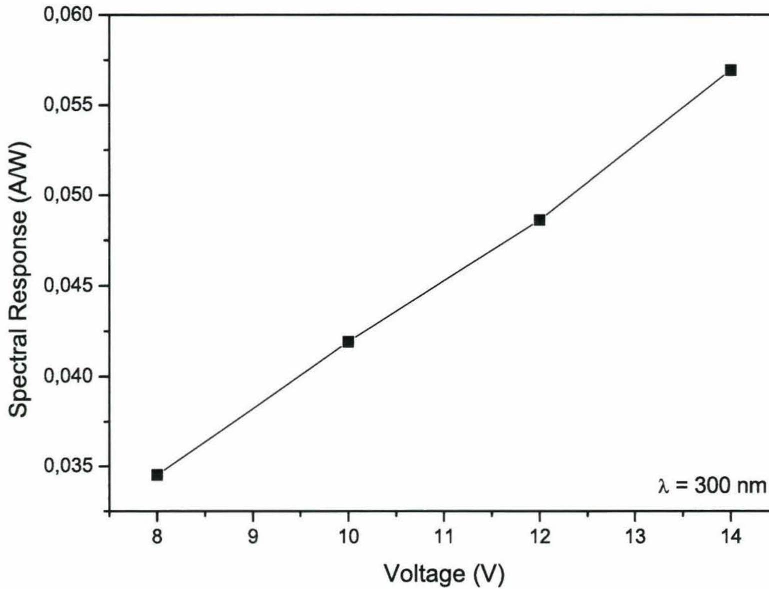

Figure 3.22: Responsivity of a 25 nm Au MSM photodetector as a function of the applied bias voltage ($\lambda = 300$ nm)

charge neutrality in the space-charge region. It is this reinjection that causes the internal gain mechanism.

3.4 The Effect of Annealing on metal/n-type GaN Schottky Barrier Diodes

Today, one of the major concerns is to reduce the dark current in GaN photodetectors or gate leakage in AlGaN/GaN High Electron Mobility Transistors (HEMTs). So far, different techniques are used with varying success to achieve this goal. For example, surface passivation using a SiO_2 or Si_3N_4 layer to reduce the gate leakage in HEMTs [24]. In that case, the dielectric layers chemically passivate the dangling bonds to reduce the surface trap density. Another method is to use wet chemical etchants like H_3PO_4 and KOH [25]. The etchants attack the defective regions and smooth the surface which decreases the leakage current. Finally, thermal annealing of the metal can also reduce the dark current due to an enhanced intimate contact between the metal and the semiconductor [26].
A detailed analysis of the influence of annealing on the Schottky parameters including the effective Richardson constant could not be found in literature. In this section, we will try to link the extracted Schottky parameters to the current transport mechanisms

and the properties of the metal-semiconductor interface. To perform this physical interpretation of the Schottky parameters, Schottky barrier diodes are prepared instead of MSM structures because the extraction of the parameters in Schottky diodes is more reliable and also the information obtained by C-V measurements can be used.
In this study, four different metallizations on the same n-type GaN ($N_d = 2.5 \times 10^{17}$ cm^{-3}) on sapphire wafer are used; Ni and Au are rather used as reference while indium-tin-oxide (ITO) and indium-tin-oxynitride (ITON) are used because both conductive materials are transparent for UV light.

ITO is a n-type degenerate semiconductor, with both oxygen vacancies and tin contributing to its high conductivity which is caused by a high carrier concentration. The high optical transmittance of ITO films is a direct consequence of the wide bandgap (3.5 eV - 4,06 eV). The fundamental absorption edge lies therefore in the ultraviolet region and shifts towards shorter wavelengths with an increase in carrier concentration due to the Burstein-Moss effect. Aperathitis *et al.* have compared the electrical an optical properties of thin ITO and ITON films [27, 28]. The films were deposited by RF-sputtering from an indium-tin-oxide target in a plasma containing pure nitrogen or Ar-N_2 mixture (ITON) or in a pure Ar plasma (ITO). Increasing the amount of nitrogen in the plasma will increase the resistivity and reduce the carrier concentration and mobility of the films. They attribute the reduced carrier concentration to the occupation of oxygen vacancies by nitrogen and the reduced mobility to the creation of defects due to the nitrogen introduction. Nevertheless, after annealing the electrical properties improve due to the outdiffusion of oxygen or nitrogen, increasing the oxygen vacancies and therefore the carrier concentration. Also, the optical properties of the ITON films improve by increasing the amount of nitrogen because the overall transmittance is inversely dependent on the free carrier concentration and thus on the conductivity. The change in the absorption edge of the ITON films deposited in pure N_2 plasma is shifted to higher energies after annealing according to the Burstein-Moss effect because the carrier concentration increases. For as-deposited ITO and ITON, they calculate an optical bandgap of 3.43 eV and 3.51 eV respectively. After annealing at 400 °C for 1 min, the bandgap increases to 3.61 eV and 3.95 eV respectively (see figure 3.23).

The enhanced UV transmittance of the ITON films is not the only reason to use them on GaN Schottky barrier devices. Another possible advantage can be the presence of nitrogen in the ITON thin films. In section 3.2.3, the thin-surface-barrier model assumes nitrogen vacancies at the surface which can act as donor and therefore enhance tunneling currents. It is likely that the outdiffusion/precense of nitrogen (after annealing) can passivate chemically the N-vacancies. So far, ITON films are never applied to Schottky barrier diodes to my knowledge.

In this study, the ITO and ITON films were deposited with a thickness of 100 nm in a 100 % Ar and a 100 % nitrogen plasma respectively with a chamber pressure of 3.0 10^{-3} mbar and 2.7 10^{-3} mbar respectively. The Ni, Au, ITO and ITON Schottky

barrier diodes were annealed from 300 °C to 600 °C each time for 15 min in a nitrogen atmosphere. The I-V characteristics of the annealed Schottky barrier photodetectors biased from -10 V to 5 V and measured at room temperature are given in figure 3.24 (Ni diodes), figure 3.25 (Au diodes), figure 3.26 (ITO diodes) and figure 3.27 (ITON diodes).

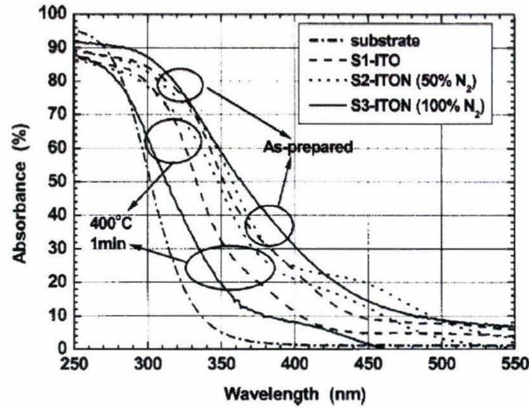

Figure 3.23: Ultraviolet absorbance spectrum of as-deposited and annealed ITO and ITON films according to Aperathitis *et al.* (From [27])

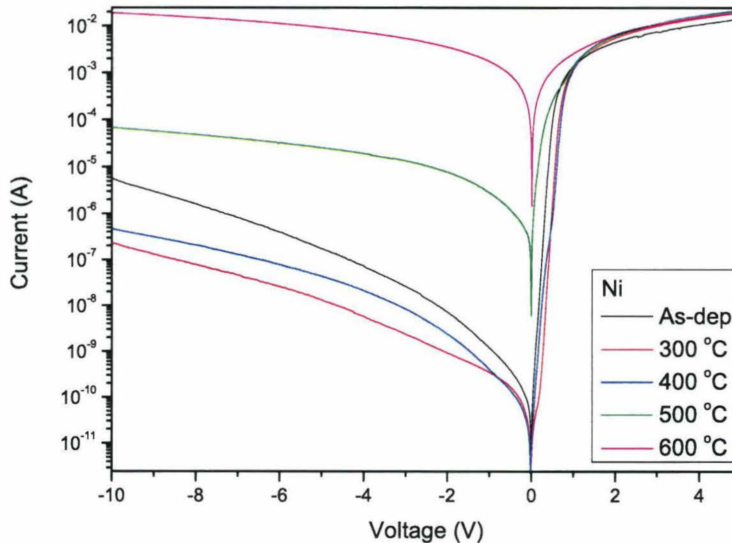

Figure 3.24: Forward and reverse I-V characteristics of Ni/n-GaN Schottky barrier diodes as function of the annealing temperature

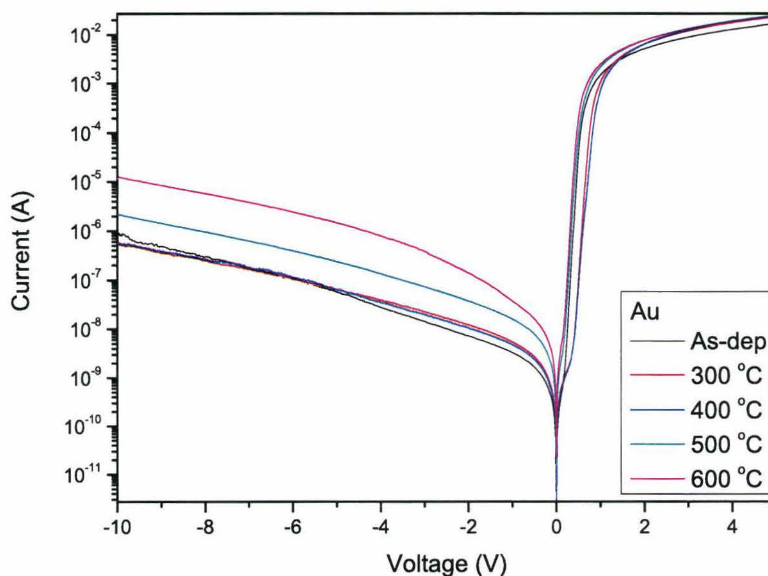

Figure 3.25: Forward and reverse I-V characteristics of Au/n-GaN Schottky barrier diodes as function of the annealing temperature

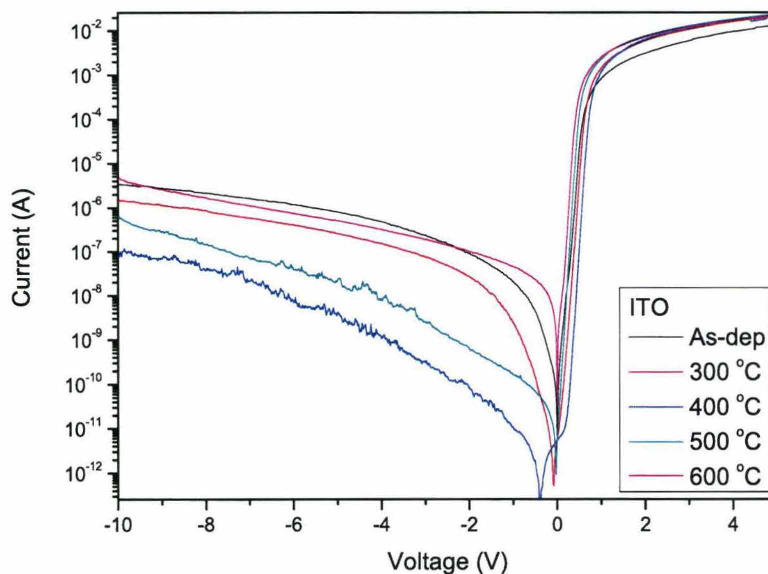

Figure 3.26: Forward and reverse I-V characteristics of ITO/n-GaN Schottky barrier diodes as function of the annealing temperature

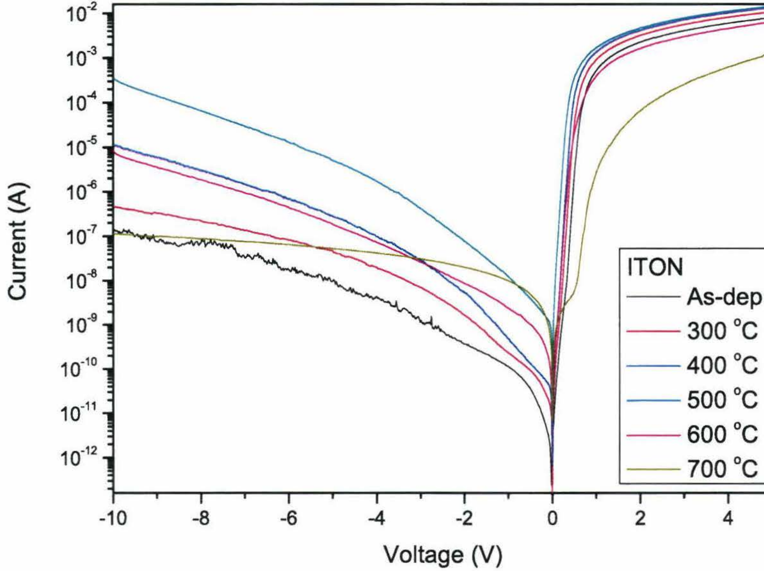

Figure 3.27: Forward and reverse I-V characteristics of ITON/n-GaN Schottky barrier diodes as function of the annealing temperature

After each annealing step, the Schottky parameters (ideality factor (n), barrier height (ϕ_B) and effective Richardson constant (A^{**})) are determined. The Schottky barrier height is extracted on two different ways by using the I-V and C-V characteristics of the Schottky barrier diodes. The barrier height is obtained from I-V measurements by extracting the reverse saturation current by extrapolating the forward-bias current in a semi-log I-V plot to V = 0V (see section 3.2.2). From the obtained slope of the forward current in a semi-log I-V plot, the ideality factor can be calculated using:

$$n = \frac{q}{k_B T} \frac{\partial V}{\partial \ln J} \tag{3.20}$$

The barrier height can also be determined by capacitance measurements using eqn. 2.9. If we assume a constant doping profile, the Schottky barrier height can be extracted from the intercept on the voltage axis according to:

$$\phi_B = V_{bi} + V_n + \frac{k_B T}{q} = V_{bi} + \frac{k_B T}{q} \ln \frac{N_c}{N_d} + \frac{k_B T}{q} \tag{3.21}$$

where V_{bi} the voltage intercept and V_n the depth of the Fermi level below the conduction band, which can be calculated if the doping concentration is known. The doping concentration can be extracted from the slope according to eqn. 2.9. The effective

Richardson constant is extracted from I-V-T measurement by making a Richardson plot (see section 3.2.2) and varying the temperature from 20 °C to 100 °C in steps of 20 °C.

The calculated Schottky parameters for the 4 different metallizations at each annealing step are summarized in table 3.3.

Metal	Annealing temperature	Ideality factor	Barrier height C-V (eV)	Barrier height I-V (eV)	Effective Richardson constant (A/cm^2K^2)
Ni	As-dep	1.27	1.00	0.59	0.027
	300 °C	1.23	1.01	0.76	0.11
	400 °C	1.43	1.12	0.65	0.012
	500 °C	n/a	1.15	n/a	n/a
	600 °C	n/a	n/a	n/a	n/a
Au	As-dep	1.17	1.05	0.69	0.056
	300 °C	1.45	1.30	0.79	0.21
	400 °C	1.61	1.40	0.74	0.082
	500 °C	1.20	1.21	0.60	0.012
	600 °C	1.17	1.15	0.62	0.061
ITO	As-dep	1.63	1.11	0.55	0.0069
	300 °C	1.38	1.22	0.65	0.011
	400 °C	1.17	1.41	0.85	0.092
	500 °C	1.11	1.30	0.64	0.018
	600 °C	1.17	1.20	0.60	0.11
ITON	As-dep	1.50	1.26	0.75	0.95
	300 °C	1.31	1.20	0.71	0.58
	400 °C	1.16	1.15	0.67	0.3
	500 °C	1.09	0.98	0.56	0.14
	600 °C	1.28	2.04	0.53	0.0024

Table 3.3: Calculated Schottky parameters for Ni, Au, ITO and ITON/n-GaN Schottky barrier diodes from I-V, I-V-T and C-V measurements as function of the annealing temperature

It can be clearly seen in table 3.3 that the Schottky barrier heights obtained from I-V measurements and C-V measurements show the same trends, but the values obtained by capacitance measurements is always higher. To know which value is the most reliable, we have to consider all the parameters which can influence the measurements. The barrier height extracted from C-V measurements is approximately the flatband barrier height because it is determined from the $1/C^2$-V curve (see eqn. 2.9) for $1/C^2 \rightarrow 0$ or $C \rightarrow \infty$, indicating sufficient forward bias to cause flatband conditions in

the semiconductor. Therefore, the Schottky barrier height obtained by capacitance measurements does not take into account the barrier height lowering because these is close to zero. The Schottky barrier lowering is given by eqn. 2.13 and is completely determined by the maximum electrical field in the semiconductor. However, when a small layer is highly doped at the metal/semiconductor interface compared to the bulk doping (thin surface barrier (TSB) model), it will induce a high(er) electrical field at the interface according to

$$E_{max} \approx \frac{qN_{DS}D}{\epsilon_s} \tag{3.22}$$

Therefore, the TSB region will cause an enhanced Schottky barrier lowering according to

$$\Delta\phi_B = \frac{q}{\epsilon_s}\sqrt{\frac{N_{DS}D}{4\pi}} \tag{3.23}$$

For $N_{DS}D = 10^{12}$ and 10^{13} cm^{-2}, the corresponding Schottky barrier lowerings are 0.045 eV and 0.14 eV respectively. These values indicate that barrier lowering play an important role to calculate the barrier height but it can not completely explain the difference between the values obtained by I-V and C-V measurements.
To extract the Schottky barrier height from I-V measurements, the effective Richardson constant has to be known. Therefore, after each annealing step the Richardson constant is extracted because the value is very sensitive to processing conditions. Nevertheless, it is still difficult to obtain a reliable value (see section 3.2.2). Hence the barrier height obtained by C-V measurements is more reliable in this case because this method is independent of the effective Richardson constant.
Also the condition of the metal-semiconductor interface is important to understand the difference in the obtained Schottky barrier heights. The annealing of the diodes can cause interfacial changes [26] and therefore can varying the C-V characteristic. Cowley [29] has shown that an interfacial layer of thickness δ and permittivity ε_i a n-type semiconductor with surface state density D_s (see section 2.3.1) produces an intercept voltage $V_{bi}^{'}$ in a $1/C^2$-V plot that is larger than the actual V_{bi}. However, the slope of the $1/C^2$-V plot remains linear with a value of $2/q\epsilon_s N_d$ as in the ideal case discussed where no interfacial layer is present. In our calculations, the obtained donor concentration from the capacitance measurements is $\pm$ 3.3 $\times$ 10^{17} cm^{-3} which is in good agreement with the predicted one. The intercept voltage $V_{bi}^{'}$ when a thin interfacial layer is present according to Cowley is given by

$$V_{bi}^{'} = V_{bi} + \alpha\sqrt{\frac{2qN_dV_{bi}}{\varepsilon_s}} + \frac{qN_d\alpha^2}{2\varepsilon_s} \tag{3.24}$$

where

$$\alpha = \frac{\delta\varepsilon_s}{\varepsilon_i + q\delta D_S} \tag{3.25}$$

From eqn. 3.24, we can conclude that the voltage intercept increases almost linear with the thickness of the interfacial layer (the last term can be neglected except at very high doping concentrations) and also a change of the effective dielectric constant

(due to annealing) can influence the voltage intercept.
As mentioned previously, a low dislocation density is crucial to achieve good quality GaN on sapphire wafers. A high density of dislocations can possibly act as current leakage paths which results in low(er) obtained Schottky barrier heights from I-V measurements. Due to lateral nonuniformity caused by the dislocations, the I-V method tends to give the lowest barrier height, where the C-V technique tends to measure more average values of the barrier height.
Therefore, we can conclude that the C-V technique gives the most reliable value of the Schottky barrier height because this method is not sensitive to the effective Richardson constant and the dislocation density but provides detailed information on the interfacial changes.
In table 3.3, it can be clearly seen that when the annealing temperatures is increased, the ideality factor decreases and the Schottky barrier height increases. Assuming that an insulating layer at the metal-semiconductor interface is present, a part of the bias voltage is dropped across the insulating layer so that the barrier height is a function of the bias voltage. The effect of this bias dependence of the barrier height is to change the shape of the I-V characteristic which is described by the ideality factor according to eqn. 3.12. Likely, annealing will promote the formation of an intimate contact between the metal and semiconductor. On the other hand, after some annealing steps (400 °C for Ni, Au and ITO) the barrier height decreases again and in general also the ideality factor increases again. A feasible explanation for this phenomenon can be the formation of an interfacial layer due to the diffusion of metal atoms in the semiconductor (for example Ni atoms into the GaN layer [30]). This can also influence the dielectric constant of the interfacial layer which influence also the ideality factor (see eqn. 3.12).
In figure 3.24 it can be seen that the Ni/n-GaN Schottky diodes loose there rectifying characteristics and become ohmic. According to eqn. 2.12, a higher Schottky barrier will reduce the saturation current density and vice versa. This relationship is clearly shown in figures 3.24 to 3.27 where the reverse saturation current decreases with increasing Schottky barrier height.

Nevertheless, the ITON/n-GaN Schottky diodes show slightly different characteristics compared to the other prepared Schottky diodes. In table 3.3, it can be seen that after the different annealing steps, the ideality factor decreases but also the Schottky barrier height decreases and this contrast with the other metallizations where annealing at 400 °C gives the lowest reverse saturation current.
First, we remark that the non-annealed ITON/n-Gan Schottky diodes have the lowest reverse saturation current ($\pm$ 10^{-7} A at 10 V). Probably, the presence of nitrogen can chemically passivate the N-vacancies which are likely present according to the TSB model and therefore it can reduce the reverse saturation current. After each annealing step, the barrier height decreases and reverse saturation current increases which can be caused to the outdiffusion of nitrogen according to Aperathitis *et al.* who also found outdiffusion of nitrogen in ITON films by performing infrared absorptions measurements. This outdiffusion can decrease the barrier height because the influence of the N-vacancies at the interface will increase. Nevertheless, at 600 °C the reverse satu-

ration current decreases suddenly 2 orders of magnitude. This phenomenon reveals itself by a increase of the Schottky barrier height obtained by capacitance measurements and a decrease of the effective Richardson constant with 2 order of magnitude. Aperathitis *et al.* observed also a shift from a crystallin to a more amorphous structure after different annealing steps (500 °C for 10 min) of ITON films deposited in pure nitrogen plasma. In our ITON/n-GaN Schottky diodes, the increased barrier height can be caused by the formation of an interfacial layer with probably a higher work-function. The formation of an interfacial layer is also in agreement with the increased ideality factor. Nevertheless, the obtained barrier height from I-V measurements is still low. This can be explained by a transition in the current transport mechanisms. The extracted effective Richardson constant in the ITO/n-GaN diodes is approximately one order of magnitude higher compared to the other metallizations. This suggest that tunneling currents are reduced in these devices. However, a large decrease of the Richardson constant is observed after annealing at 600 °C. According to Libra *et al.*, the amorphous structure in ITO films generally contains levels of localized states lying near the forbidden gap edges in the band structure [31]. Therefore, it is likely that these introduced traps in the ITON films play an important role in the current transport mechanisms and reduce the effective Richardson constant. The influence of these traps is also visible in the UV response of the ITON/n-GaN Schottky barrier diodes annealed at 600 °C for 15 min (see figure 3.28).

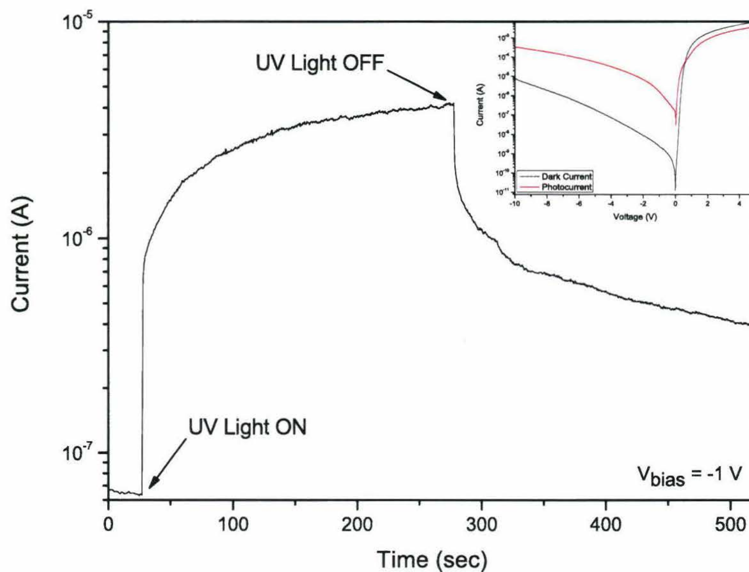

Figure 3.28: UV response (UV light off → UV light on → UV light off) of a ITON/n-Gan Schottky barrier diode annealed at 600 °C for 15 min at a bias voltage of -1 V. The inset shows the I-V characteristic in dark and under illumination.

We already reported in section 3.3 that photo-generated carriers can cause a decreased barrier height due to the conservation of charge neutrality which can be disturbed by trapped charge carriers. To examine this hypothesis, capacitance measurements were performed at ITON/n-GaN Schottky diodes annealed at 400 °C in dark and under UV illumination (see figure 3.29).

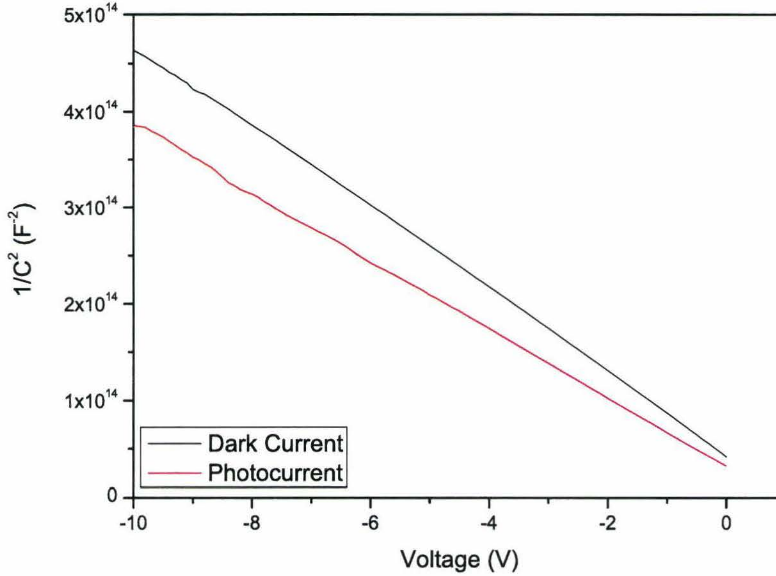

Figure 3.29: $1/C^2$-V characteristic of ITON/n-GaN Schottky diodes annealed at 400 °C in dark and under UV illumination showing a different Schottky barrier height due to a different voltage intercept

When the ITON/n-GaN Schottky diodes are UV illuminated, the barrier height obtained from the C-V measurements decreases 0.21 eV from 1.15 eV to 0.94 eV.
We know that in n-type GaN a number of generation-recombination centers or traps could be present due to the many threading edge dislocations or nitrogen vacancies which are acting as donors in n-type GaN. Also the localized states lying in the bandgap caused by amorphous thin films and surface/interface states can act as traps. Depending on the photon-energy, the light source can create electron-hole pairs (photon energy above the band gap) that will be separated by the depletion region and therefore creating a photovoltage (see inset figure 3.28) but it can also ionize some interface traps even for photon energies below the bandgap. In that case, the equilibrium surface charge is affected due to a reduction of trapped electrons. Therefore the depletion width has to be reduced which will cause a lower Schottky barrier height. The barrier lowering is therefore proportional to the occupied trap concentration.

When the light source is switched off, the photocurrent decreases because the capture flux is larger than the emission rate and an electron recapture process will start to reoccupy the traps and therefore the Schottky barrier height recovers again. This persistent photocurrent (PPC) effect can be clearly seen in figure 3.28. On the other hand, the turn-on transient is much faster. This is likely caused due to the higher involved electron fluxes.
At this moment, two current mechanisms are contributing to the photocurrent. The first is the photocurrent caused by charge carriers optically generated in the depletion region. The second photocurrent is due to the lowering of the Schottky barrier caused by illumination and trapping of the carriers. This mechanisms is responsible for the gain, which can be seen in the spectral response of the ITON/n-GaN Schottky diodes (figure 3.30).

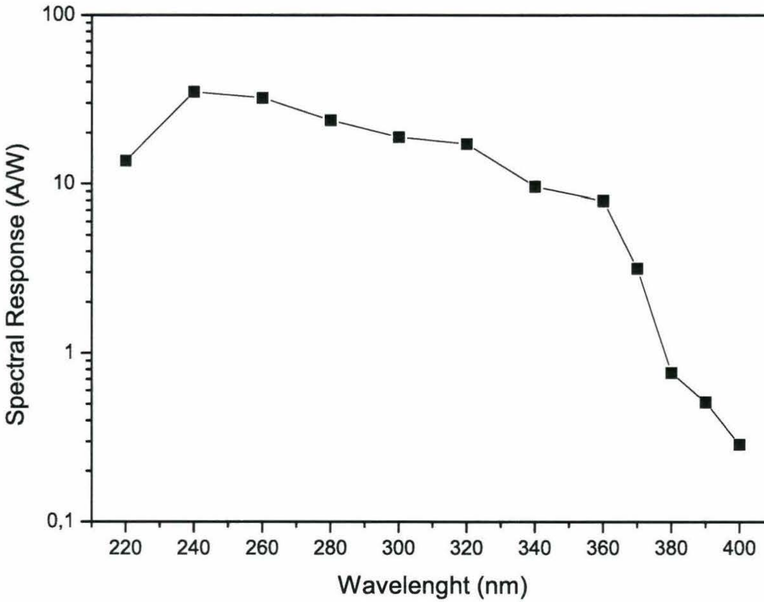

Figure 3.30: Spectral response of a ITON/n-GaN Schottky barrier diode annealed at 500 °C (V_{bias} = -1 V)

According to eqn. 3.17 and assuming 100 % quantum efficiency, the maximum responsivity is approximately 0.3 A/W. Therefore, it is clear that gain mechanisms are responsible for the high response of these photodetectors. Nevertheless, these enhanced photo-to-dark current ratio due to the Schottky barrier lowering and trapping of the charge carriers will limit the bandwidth (Δf) of the photodetectors where

$$\Delta f = \frac{1}{2\pi\tau} \tag{3.26}$$

where τ the typical time constant for the photodetector to reach the steady-state dark current after switching of the UV illumination. In figure 3.28, it is clear that this time constant is in the order of 10^2 seconds. On the other hand, the prepared MSM photodetectors and non-annealed ITO or ITON/n-GaN Schottky barrier diodes show significantly smaller time constants of approximately 1 second.

Chapter 4

Conclusions and Outlook

In this study, a detailed electrical and optical characterization of MSM structures as photodetectors is performed. Due to the lack of good quality p-type GaN material and good ohmic contacts, GaN MSM structures are the first option to fabricate UV photodetectors. Also the fabrication simplicity, low capacitance and low dark current density are major advantages of MSM photodetectors.
According to the MSM theory, three operation regions (low-current, injection and saturation region) are distinguished as function of the applied voltage. In our MSM photodetectors only the saturation region is present which is proved by capacitance measurements. This is caused by the small donor concentrations ($\pm\ 10^{16}$ cm^{-3}) and the small spacing between the interdigitated metal contacts. The dark current in the saturation is almost completely determined by electrons. Due to the large bandgap of GaN (E_g = 3.4 eV), the decreasing hole barrier in the injection and saturation region is still to high for the holes to have a significant contribution to the dark current. Nevertheless, a saturation of the dark current is not observed in our MSM photodetectors.

To investigate and model the current transport mechanisms which are involved in the dark current, first the Schottky parameters (Schottky barrier height and effective Richardson constant) have to be determined from the MSM I-V-T characteristics. The extracted effective Richardson constant was two or three orders of magnitude smaller than the theoretical one. Theoretically, the Richardson constant is a material constant and therefore should be independent on metallization but this was not observed in our MSM photodetectors. The small effective Richardson constant can be an indication for large tunneling or leakage currents. However, a large error in the extraction of the effective Richardson constant is introduced to the variability of the MSM active area and the small temperature range of the Richardson plot. The Richardson plot is based on the thermionic emission theory and therefore when large tunneling current are present, the calculated effective Richardson constant is 1 order smaller than the real one. The calculated effective Richardson constant is also important to extract the Schottky barrier height from I-V measurements. Due to the lack of current saturation, the extraction of the barrier height by extrapolation of the $\ln(I)$ versus V plot to V =

0V is not reliable. Nevertheless, the Norde method can determine reliably the Schottky barrier height because these method extract accurately the reverse saturation current at low applied voltage in contrast with the method supposed by Averine *et al.* [13].

To investigate which current transport mechanisms are responsible for the lack of saturation, different theoretical models are compared with the measured dark current. The measured dark current do not show the same characteristics compared to the MSM theory which is based on thermionic emission with Schottky barrier lowering. Possibly, also generation-recombination currents do not contribute to the dark current due to the large bandgap of GaN. In general, large dislocation densities (10^8 - 10^{10} cm^{-2}) are present in GaN on sapphire wafers due to large lattice and thermal mismatch between these materials. A large concentration of (threading edge) dislocations introduces states in the forbidden bandgap and they can act as traps. These traps will promote trap-assisted tunneling as current transport mechanisms. This mechanism agree qualitatively with the observed hysteresis effects by subsequent measuring the MSM photodetectors in dark and under white light illumination. An initial dark current measurements can occupy some traps, whereas measurements under white light can empty traps due to the visible and IR light components. Nevertheless, MSM photodetectors on different wafers do not shown these hysteresis effects. This suggests that the quality of the wafers (low dislocation density) is one of the most important parameters to achieve high performance MSM photodetectors. We believe that these measured dark currents can be qualitatively and quantitatively explained using the thin surface barrier (TSB) model. This model assumes a thin region at the surface with a higher donor concentration compared to the bulk concentration. These high donor concentration at the surface can be caused due to the presence of nitrogen vacancies caused by metal deposition. This thin layer will enhance tunneling currents and can therefore explain the lack of saturation. It can also explain the large scatter in measured dark current densities because the parameter choice of the donor concentration and the thickness of the thin layer is very critical.

To investigate which current mechanisms determine the photocurrent, I-V-T and capacitance measurements on ultraviolet illuminated MSM photodetectors are performed. Both measurements show a decreased barrier height compared to the dark condition. Interface or defect states can trap the photo-generated charge carriers and therefore disturb the charge neutrality condition at the surface. To satisfy this condition again, the depletion region and therefore the barrier height has to be reduced. This effect has two consequences. First, a photoconductive gain is introduced due to the subsequent re-emission of the charge carriers. Secondly, after switching of the UV illumination, the charge carriers has to re-occupy the traps again to satisfy the charge neutrality condition at the interface. This will introduce a persistent photocurrent (PPC) effect which is dependent on the occupied trap concentration and the trap time constants. In conclusion, the photocurrent to dark current ratio will increase due to the gain effect but the bandwidth/speed of the photodetector will decrease. The responsivity of the prepared Au MSM photodetector is 0.03 A/W which give a quantum efficiency

of approximately 15 % if no gain is taken into account.

Annealing of Schottky contacts is one method to decrease the dark current. Annealing will enhance the formation of an intimate contact between the metal and semiconductor. This reveals itself in a higher Schottky barrier height and a decreased ideality factor which leads to a reduced reverse saturation current in Schottky barrier diodes. Also the calculated effective Richardson constant is important because this value gives an indication (of the change) of the current transport mechanisms.
The use of other Schottky contacts can also decrease the dark current. A promising candidate is indium-tin-oxynitride (ITON) not only due to the enhanced transparency in the ultraviolet region compared to indium-tin-oxide (ITO) but also the presence of nitrogen in these thin films can chemically passivate the GaN surface according to the nitrogen vacancies introduced in the thin surface barrier (TSB) model. As-deposited ITON films show the most promising result due to the lowest reverse saturation currents compared to other metallizations and the high responsivity to UV illumination. Annealing of the ITON films will cause outdiffusion of nitrogen resulting in a lower barrier height and will also create traps due to the creating of states in the forbidden bandgap due to the transition of a crystalline into an amorphous structure. The latter will limit the operating speed of the photodetector.

Another more structural method to avoid the surface/interface problems which are discussed above is to change the device structure by using p-n junctions as photodetectors. In that case, the saturation voltage is some order of magnitude smaller compared to Schottky barrier devices and most important, the operation region is shifted from the surface (Schottky barrier device) to the bulk of the photodetector. Therefore, the material quality is critical to achieve high performance p-n UV photodetectors. Particulary, high quality p-type GaN is the most important condition to achieve long diffusion lengths and high mobility of the minority carriers.

References

[1] L. Liu, J.H. Edgar. Substrates for gallium nitride epitaxy. *Materials Science and Engineering*, R 37:61–127, 2002.

[2] E. Monroy, F. Omnes, F. Calle. Wide-bandgap semiconductor ultraviolet photodetectors. *Semiconductor Science and Technology*, 18:R33–R51, 2003.

[3] Chris G. Van de Walle, Jorg Neugebauer. First-principles calculations for defects and impurities: Applications to III-nitrides. *Journal of Applied Physics*, 95:3851–3879, 2004.

[4] S.M. Sze. *Physics of Semiconductor Devices.* Wiley-Interscience, 1981.

[5] E.H. Rhoderick & R.H. Williams. *Metal-Semiconductor Contacts.* Oxford University Press, New York, 1988.

[6] S.M. Sze, D.J. Coleman, JR. and A. Loya. Current transport in metal-semiconductor-metal (MSM) structures. *Solid-State Electronics*, 14:1209–1218, 1971.

[7] L. Liou, B. Nabet. Simple analytical model of bias dependence of the photocurrent of metal-semiconductor-metal photodetectors. *Applied Optics*, 35:15–23, 1996.

[8] K. Honkanen. *Fabrication and modelling of SOI and GaAs MSM photodetectors and a GaAs-based integrated photoreceiver.* PhD thesis, Helsinki University of Technology, 2001.

[9] Z.P. Guan, J.Z. Li, G.Y. Zhang, S.X. Jin, X.M. Ding. Minority electron mobility in a p-n GaN photodetector. *Semiconductor Science and Technology*, 15:51–54, 2000.

[10] C.R. Crowell, S.M. Sze. Current transport in metal-semiconductor barriers. *Solid-state Electronics*, 9:1035–1048, 1966.

[11] Dieter K. Schroder. *Semiconductor material and device characterization.* Wiley-Interscience, 1998.

[12] L.S. Yu, Q.Z. Liu, Q.J. Xing, D.J. Qiao, S.S. Lau, J. Redwing. The role of the tunneling component in the current-voltage characteristics of metal-GaN Schottky diodes. *Journal of Applied Physics*, 84:2099–2104, 1998.

[13] S. Averine, Y.C. Chan, Y.L. Lam. Evaluation of Schottky contact parameters in metal-semiconductor-metal photodiode structures. *Applied Physics Letters*, 77:274–276, 2000.

[14] B. Akkal, Z. Benamara, H. Abid, A. Talbi, B. Gruzza. Electrical characterization of Au/n-GaN Schottky diodes. *Materials Chemistry and Pysics*, 85:27–31, 2004.

[15] H. Norde. A modified forward I-V plot for Schottky diodes with high series resistance. *J. Appl. Phys.*, 50:5052–5053, 1979.

[16] T. Sawada, Y. Ito, K. Imai, K. Suzuki, H. Tomozawa, S. Sakai. Electrical properties of metal/GaN and SiO_2/GaN interfaces and effect of thermal annealing. *Applied Surface Science*, 159-160:449–455, 2000.

[17] E.G. Brazel, M.A. Chin, V. Narayanamurti. Direct observation of localized high current densities in GaN films. *Applied Physics Letters*, 74:2367–2369, 1999.

[18] J.C. Carrano, T. Li, P.A. Grudowski, C.J. Eiting, R.D. Depuis, J.C. Campbell. Comprehensive characterization of metal-semiconductor-metal ultraviolet photodetectors fabricated on single-crystal GaN. *Journal of Applied Physics*, 83:6148–6160, 1998.

[19] S.C. Binari, H.B. Dietrich, W. Kruppa, G. Kelner, N.S. Saks, A. Edwards, J.M. Redwing, A.E. Wickenden, D.D. Koleske. GaN-based electronic devices for high-power, high-speed, and high-temperature applications. In *Proceedings of the Second International Conference on Nitride Semiconductors*, pages 476–478, 1997.

[20] H. Hasegawa, S. Oyama. Mechanism of anomalous current transport in n-type GaN Schottky contacts. *J. Vac. Sci. Technol. B*, 20:1647–1655, 2002.

[21] K. Leung, A.F. Wright, E.B. Stechel. Charge accumalation at a threading edge dislocation in gallium nitride. *Applied Physics Letters*, 74:2495–2497, 1999.

[22] D. Volm, K. Oettinger, T. Streibl, D. Kovalev, M. Ben-Chorin, J. Diener, B.K. Meyer. Exciton fine structure in undoped GaN epitacial films. *Physical Review B*, 53:16543–16550, 1996.

[23] Shun Lien Chuang. *Physics of Optoelectronic Devices*. Wiley Series in Pure and Applied Optics, 1995.

[24] W.S. Tan, P.A. Houston, P.J. Parbrook, G. Hill and R.J. Airey. Comparison of different surface passivation dielectrics in AlGaN/GaN heterostructure field-effect transistors. *Journal of Physics D: Applied Physics*, 35:595–598, 2002.

[25] J. Spradlin, S. Dogan, M. Mikkelson, D. Huang, L. He, D, Johnstone, H. Morkoç, R.J. Molnar. Improvement of n-GaN Schottky diode rectifying characteristics using KOH etching. *Applied Physics Letters*, 82:3556–3558, 2003.

[26] S. Arulkumaran, T. Egawa, H. Ishikawa, M. Umeno, and Takashi Jimbo. Effects of Annealing on Ti, Pd, and Ni/n-$Al_{0.11}Ga_{0.89}N$ Schottky Diodes. *IEEE Transactions on Electron Devices*, 48:573–580, 2001.

[27] E. Aperathitis, M. Bender, V. Cimalla, G. Ecke, M. Modreanu. Properties of rf-sputtered indium-tin-oxynitride thin films. *Journal of Applied Physics*, 94:1258–1266, 2003.

[28] E. Aperathitis, M. Modreanu, M. Bender, V. Cimalla, G. Ecke, M. Androulidaki, N. Pelekanos. Optical characterization of indium-tin-oxynitride fabricated by RF-sputtering. *Thin Solid Films*, 450:101–104, 2004.

[29] A.M. Cowley. Depletion Capacitance and Diffusion Potential of Gallium Phosphide Schottky-Barrier Diodes. *Journal of Applied Physics*, 37:3024–3032, 1966.

[30] J.D. Guo, F.M. Pan, M.S. Feng, R.J. Guo, P.F. Chou, C.Y. Chang. Schottky contact and the thermal stability of Ni on n-type GaN. *Journal of Applied Physics*, 80:1623–1627, 1996.

[31] M. Libra, L. Bardos. Effect of post-deposition vacuum annealing on properties of ITO layers. *Vacuum*, 38:455–457, 1998.

Appendix A

Detailed Process Flow Photodetectors

In this appendix, the processing details to fabricate the MSM and Schottky barrier photodectors with all the cleaning and photolithography procedures ara given.

A.1 MSM Photodetectors

Step 1: Dicing 2 inch GaN wafer and alignment crosses

- Protection for dicing GaN wafer: Litho: S1828, 4000 rpm, 1 min at 120 °C on hotplate
- Dicing GaN wafer in 4 quarters
- Strip of resist and cleaning: Aceton in beaker, 1 min hot aceton, 1 min hot IPA, DI water, nitrogen drying
- Litho for alignment crosses
  - ma-N420 / 4000 rpm / 30 sec
  - Softbake at 90 °C for 2.30 min on hotplate
  - 25 sec exposure on MA6 with hard contact
  - Development in OPD 5262 for 2 min
- Metallization: RF-sputtering of TiW/Au (10/160 nm)
- Lift-off metallization

Step 2: Finger structures

- Cleaning: 1 min hot aceton, 1 min hot IPA, DI water, nitrogen drying
- RF-sputtering metallization (Au or Pt)

- Litho for patterning MSM structures
  - S1828 / 4000 rpm / 30 sec
  - Softbake 1 min at 120 °C on hotplate
  - 15 sec exposure on MA6 with hard contact
  - 2*40 sec development in DEV .351 (diluted 1:4 with water)
- Oxygen plasma treatment (100 W/ 1 min)
- Wet ecth 25 sec (diluted 1:8 Au 5-solution with water)
- Strip of resist in aceton beaker

Step 3: Contacts pads

- Cleaning: 1 min hot aceton, 1 min hot IPA, DI water, nitrogen drying
- Litho for contacts pads
  - S1828 / 4000 rpm / 30 sec
  - Softbake 1 min at 120 °C on hotplate
  - 15 sec exposure on MA6 with hard contact
  - 2*40 sec development in DEV .351 (diluted 1:4 with water)
- Metallisation: RF-sputtering TiW/Au (10/160 nm)
- Lift-off metallization

A.2 Schottky Barrier Photodetectors

Step 1: Dicing 2 inch GaN wafer and alignment crosses

- Protection for dicing GaN wafer: Litho: S1828, 4000 rpm, 1 min at 120 °C on hotplate
- Dicing GaN wafer in 4 quarters
- Strip of resist and cleaning: Aceton in beaker, 1 min hot aceton, 1 min hot IPA, DI water, nitrogen drying
- Litho for alignment crosses
  - S1828 / 4000 rpm / 30 sec
  - Softbake at 120 °C for 1 min on hotplate
  - 15 sec exposure on MA6 with hard contact
  - 2*40 sec development in DEV .351 (diluted 1:4 with water)

- Metallization: RF-sputtering of TiW/Au (10/160 nm)
- Lift-off metallization

Step 2: Ohmic contacts

- Cleaning: 1 min hot aceton, 1 min hot IPA, DI water, nitrogen drying
- Litho for ohmic contacts
  - ma-N420 / 4000 rpm / 30 sec
  - Softbake 2.30 min at 90 °C on hotplate
  - 25 sec exposure on MA6 with hard contact
  - Development in OPD 5262 for 2 min
- Metallization: RF-sputtering of Ti/Al/Mo/Au (20-40-25-50 nm) alloy
- Lift-off metallization
- Annealing of the ohmic contacts: 15 min at 550 °C and 1 min at 750 °C

Step 3: Schottky contacts

- Cleaning: 1 min hot aceton, 1 min hot IPA, DI water, nitrogen drying
- Litho for Schottky contacts
  - S1828 / 4000 rpm / 30 sec
  - Softbake 1 min at 120 °C on hotplate
  - 15 sec exposure on MA6 with hard contact
  - 2*40 sec development in DEV .351 (diluted 1:4 with water)
- Metallization: RF-sputtering of the different metals
- Lift-off metallization

Appendix B

IGOR Pro Procedure Files

In this appendix, the procedure files used in IGOR Pro to model and fit the measured I-V characteristics of the MSM photodetectors are given using the thermionic emission theory with barrier lowering, thermionic-field emission and the thin surface barrier (TSB) model.

B.1 Thermionic Emission with Barrier Lowering

```
Function TElow(w,V) : FitFunc
    Wave w
    Variable V


Variable area, q, es, pi, k, T, s, delta, J
Variable phi, A, nd
phi = w[0]
A = w[1]
nd = w[2]

area=0.00025
q = 1.6e-19
h = 6.6262e-34
es = 8.4075e-13
pi = 3.1415
k = 1.38e-23
T = 293.15
s = 8e-4

delta=sqrt(q*((V-(q*nd*s^2)/(2*es)))/(4*pi*es*s))
J=A*area*T^2*exp(-q*phi/(k*T))*exp(q*delta/(k*T))
```

```
return J


End
```

B.2 Thermionic-Field Emission

```
Function TFEreverse(w,V) : FitFunc
    Wave w
    Variable V


Variable area, q, h, m, es, k, T, nc, Vn, E0, Js, J
Variable phi, A, nd
phi = w[0]
A = w[1]
nd = w[2]

area=0.00025
q = 1.6e-19
h = 6.6262e-34
m = 2.00409e-31
es = 8.4075e-13
k = 1.38e-23
T = 293.15

nc = (4.3e14)*T^(3/2)
Vn=phi-(k*T*ln(nc/nd))/q
E0=q*h*sqrt(nd/(m*es))/2
Js=((A*T*sqrt(pi*E0))/k)*(sqrt(abs((q*(V-Vn)+
((q*phi)/((cosh(E0/(k*T)))^2)))))*exp((-q*phi)/(E0*(1/tanh(E0/(k*T))))))
J=area*Js*exp(((q*V)/E0)*((E0/(k*T))-tanh(E0/(k*T))))

return J


End
```

B.3 Thin Surface Barrier (TSB) model

```
Function TSBr(w,V) : FitFunc
    Wave w
    Variable V
```

```
Variable area, q, h, nd, m, es, k, T, nc, Vn, V0, E0, phi0, Js, J
Variable phi, nds, d, A

phi = w[0]
nds = w[1]
d = w[2]
A = w[3]

T = 293.15
area=0.00025
nd = 1e16
q = 1.6e-19
h = 6.6262e-34
m = 2.00409e-31
es = 8.4075e-13
k = 1.38e-23

nc = (4.3e14)*T^(3/2)
Vn=(k*T*ln(nc/nd))/q
V0=phi-(q*nds*d^2)/(2*es)-Vn
E0=q*(h/(2*pi))*sqrt(nds/(m*es))/2
phi0=(q*nd/(2*es))*(1-(nd/nds))*
(sqrt((((2*es/(q*nd))*(V0-V)+d^2)))-d)^2+V+Vn
Js=((A*T*sqrt(pi*E0))/k)*(sqrt(abs((q*(V-Vn)+
((q*phi)/((cosh(E0/(k*T)))^2)))))*exp((-q*phi0)/(E0*(1/tanh(E0/(k*T))))))
J=area*Js*exp(((q*phi0)/E0)*((E0/(k*T))-tanh(E0/(k*T))))

return J


End
```